remote sensing

MDPI

Article

Surface and Interior Dynamics of Arctic Seas Using Surface Quasi-Geostrophic Approach

Marta Umbert [1,2,*], Eva De-Andrés [1,3], Rafael Gonçalves-Araujo [4], Marina Gutiérrez [5], Roshin Raj [6], Laurent Bertino [6], Carolina Gabarró [1,2] and Jordi Isern-Fontanet [1,2]

1 Department of Physical and Technological Oceanography, Institut de Ciències del Mar, CSIC, 08003 Barcelona, Spain
2 Barcelona Expert Center on Remote Sensing, CSIC-UPC, 08003 Barcelona, Spain
3 Department of Applied Mathematics, Universidad Politécnica de Madrid, 28040 Madrid, Spain
4 National Institute of Aquatic Resources, Technical University of Denmark, DTU Aqua, 2800 Lyngby, Denmark
5 Departamento de Física, Universidad Las Palmas de Gran Canaria (ULPGC), 35017 Las Palmas de Gran Canaria, Spain
6 Nansen Environmental and Remote Sensing Center (NERSC) and Bjerknes Center for Climate Research, 5007 Bergen, Norway
* Correspondence: mumbert@icm.csic.es

Abstract: This study assesses the capability of Surface Quasi-Geostrophy (SQG) to reconstruct the three-dimensional (3D) dynamics in four critical areas of the Arctic Ocean: the Nordic, Barents, East Siberian, and Beaufort Seas. We first reconstruct the upper ocean dynamics from TOPAZ4 reanalysis of sea surface height (SSH), surface buoyancy (SSB), and surface velocities (SSV) and validate the results with the geostrophic and total TOPAZ4 velocities. The reconstruction of upper ocean dynamics using SSH fields is in high agreement with the geostrophic velocities, with correlation coefficients greater than 0.8 for the upper 400 m. SSH reconstructions outperform surface buoyancy reconstructions, even in places near freshwater inputs from river discharges, melting sea ice, and glaciers. Surface buoyancy fails due to the uncorrelation of SSB and subsurface potential vorticity (PV). Reconstruction from surface currents correlates to the total TOPAZ4 velocities with correlation coefficients greater than 0.6 up to 200 m. In the second part, we apply the SQG approach validated with the reanalysis outputs to satellite-derived sea level anomalies and validate the results against in-situ measurements. Due to lower water column stratification, the SQG approach's performance is better in fall and winter than in spring and summer. Our results demonstrate that using surface information from SSH or surface velocities, combined with information on the stratification of the water column, it is possible to effectively reconstruct the upper ocean dynamics in the Arctic and Subarctic Seas up to 400 m. Future remote sensing missions in the Arctic Ocean, such as SWOT, Seastar, WaCM, CIMR, and CRISTAL, will produce enhanced SSH and surface velocity observations, allowing SQG schemes to characterize upper ocean 3D mesoscale dynamics up to 400 m with higher resolutions and lower uncertainties.

Keywords: ocean currents; Arctic; ocean dynamics; Surface Quasi-Geostrophy; sea surface height; remote sensing; physical oceanography

check for updates

Citation: Umbert, M.; De Andrés, E.; Gonçalves-Araujo, R.; Gutiérrez, M.; Raj, R.; Bertino, L.; Gabarró, C.; Isern-Fontanet, J. Surface and Interior Dynamics of Arctic Seas Using Surface Quasi-Geostrophic Approach. *Remote Sens.* **2023**, *15*, 1722. https://doi.org/10.3390/rs15071722

Academic Editors: Daniele Ciani and Milena Menna

Received: 13 February 2023
Revised: 16 March 2023
Accepted: 21 March 2023
Published: 23 March 2023

Copyright: © 2023 by the authors. Licensee MDPI, Basel, Switzerland. This article is an open access article distributed under the terms and conditions of the Creative Commons Attribution (CC BY) license (https://creativecommons.org/licenses/by/4.0/).

1. Introduction

Changes in the hydrography of the upper Arctic Ocean, a hotspot for climate change, have been observed in recent observational and modeling studies. In particular, an increase in its liquid freshwater content, shifts in frontal locations and ocean currents, such as the intensification of the anticyclonic circulation in the Beaufort Gyre, or the shift of the transpolar drift have been described in the last decade [1–4]. An increase in the summer geostrophic currents of the Beaufort Gyre was linked to sea ice melt in the Beaufort Sea throughout the 2000s [5], evidencing the effects of climate change in high-latitude ocean

dynamics. Through feedback mechanisms and interactions with the northern hemisphere's atmospheric circulation, retreating sea ice cover, and the associated warmer and fresher upper ocean have a widespread impact across the entire Arctic system. By intensifying the stratification of the water column, the changing freshwater distribution has the potential to destabilize the thermohaline circulation, which distributes heat from the tropics to the polar regions [5–7]. Ocean currents of the upper ocean, along with wind and waves, play a fundamental role in the formation of sea ice, the dispersion of ice floes, and the dynamics of ice growth and shrinking. Being able to depict and predict upper ocean circulation at high latitudes accurately is critical to provide a better understanding of the processes underlying the dynamics of the coupled ocean–ice–atmosphere system's variability, its effects on the global climate, and its implications in accessing and navigating the Arctic as sea ice retreats [8–10].

The Subarctic Seas constitute the northern part of the thermohaline circulation, which regulates the Earth's climate. Through the Nordic Seas, warm and saline Atlantic water is transported from the North Atlantic to the Arctic. The Nordic Seas are a sensitive area in the Arctic Ocean, where the inflow of freshwater from melting Arctic ice enhances surface water stratification and could modify deep convection processes, weakening deep water overflows along the Greenland–Scotland Ridge [11] and the formation of the North Atlantic Deep Water [12,13]. The Nordic Seas' main oceanographic features include the warm and saline Atlantic water, flowing northward along the Nordic Seas' eastern boundary, and the cold and comparatively fresh polar water, entering through the Fram Strait (FS in Figure 1) and flowing southward along the Nordic Seas' western boundary [14]. The Atlantic water (AW in Figure 1) is transported into the Nordic Seas and flows northward via the two branches of the Norwegian Atlantic Current (NwAC in Figure 1). The eastern branch flows along the shelf edge as a barotropic slope current (Norwegian Atlantic Slope Current; NwASC), while the western branch follows the western rim of the Norwegian Sea as a topographically guided front current (Norwegian Atlantic Front Current; NwAFC). On its way northward, the NwASC bifurcates into two, one part flowing into the Barents Sea (BaS) and the other part continuing towards the Fram Strait as the core of the West Spitsbergen Current. Only a part of the Atlantic water transported into the Nordic Seas enters the Arctic Ocean along the eastern side of the Fram Strait, forming the Atlantic Intermediate Layer. The rest of the Atlantic water recirculates southward to the Greenland Sea along the East Greenland Current (EGC in Figure 1), underneath the cold and fresh polar surface waters that arrive from the transpolar drift (TD in Figure 1) and sea ice. This EGC current also carries intermediate and deep waters from the Arctic Ocean [15]. The Atlantic water that enters the Barents Sea, which serves as the Arctic Ocean's cooling machine, dissipates the majority of the incoming heat transported by the slope current. As a result, the Atlantic water transported into this region densifies and finally flows to the intermediate and deeper layers of the Arctic Ocean. According to [16], the cooling machine has moved poleward from the Barents to the Kara Sea as the temperature has been rising due to climate change. As a result, the Arctic Atlantification will be strengthened and pushed poleward in the future [17].

Apart from the influence of AW transported from the Nordic Seas, the upper Arctic Ocean is largely influenced by the transport and transformation of water masses happening in the East Siberian Seas (ESS) [4], where the Arctic halocline water is partly produced [18]. The ESS is characterized by a buoyancy-driven eastward-flowing boundary current, which transports low-salinity and low-temperature waters from great Russian river discharges. Freshwater changes in the ESS reflect changes in the transpolar drift axis (TD in Figure 1) counterclockwise from the Eurasian to the Canadian Basin [1], driving Russian runoff east to the Canadian Basin. On the western side of the Arctic Ocean, the freshwater is accumulated in the anticyclonic Beaufort Gyre (BG in Figure 1). The BG is driven by the anticyclonic wind stress curl forced by a high-pressure system in the lower atmosphere [19,20]. Closer to the coast, we found the cyclonic, topographically steered Beaufort shelf-break current [21]. The BG is the largest Arctic Ocean freshwater reservoir and has drastically increased its

liquid freshwater content by 40% in the past two decades [22,23]. The main contributors to the accumulated freshwater in the BG are the sea ice meltwater, the influence of freshwater arriving from the Russian side, and the Mackenzie river runoff [24,25]. Freshwater accumulates in the interior of the BG through Ekman convergence and leaves the Arctic through the Davis and the Fram Straits.

The difficult environmental conditions of the Arctic make remote sensing a good alternative to in-situ measurements of ocean currents [26]. Indeed, in the last thirty years, different remote sensing approaches have provided regular measurements of key variables such as the sea surface temperature (SST) and sea surface height (SSH). Moreover, the launch of the Soil Moisture and Ocean Salinity (SMOS) mission more than ten years ago has added the sea surface salinity (SSS) to the routinely observed variables in the Arctic [27,28]. Surface currents are routinely estimated operationally by applying geostrophic and hydrostatic principles to satellite altimetry data collected using satellite altimeters such as ERS-1, Jason 3, Sentinel 3, Sentinel 6, CryoSat-2, or ICESat-2 [29,30]. The methodology assumes that the flow in the ocean interior is the first order in the geostrophic balance, and the gradients of the ocean dynamic topography are used to estimate the ocean surface velocity field. The expected spatial scales of geostrophic structures in the ocean, which is defined by the first baroclinic Rossby radius, is on average 5–15 km and does not exceed 16 km at high latitudes [31,32]. Satellite altimetry offers global, precise, and repeated measurements of the ocean's dynamic topography; however, the nadir altimeter-based estimations do not resolve scales lower than 100 km and 10 days, and they have substantial errors in the shelf seas (where tides and wind-driven dynamics predominate) and near the ice edge [33,34]. The mapping capability of the present altimeter constellation, coupled with the resolution and accuracy of the available Mean Dynamic Topography (MDT) products [35], is limited to resolving the full geostrophic flow at high latitudes [36,37]. Some upcoming missions will improve the monitoring of polar regions by directly measuring surface currents (Seastar [38,39] and WaCM [40]) or improving our capability to measure SSH (SWOT [41,42] and CRISTAL [43]). All of them, existing and new missions, would benefit polar oceanography by improving the capacity of monitoring ocean currents, but they have in common that they provide information on the ocean surface but not on the three-dimensional structure of the upper Arctic Ocean.

The reconstruction of the ocean interior from satellite observations requires additional assumptions [44,45]. In 2006, it was proposed to use the Surface Quasi-Geostrophic (SQG) theory to obtain estimations of subsurface dynamics from satellite measurements [46,47]. The validity of this approach was tested using infrared SST [48–50]; microwave [51,52]; and SSS [53] measurements. The main conclusion was that the SQG approach is better suited to reconstruct the ocean dynamics in the upper 500 m for energetic areas with deep mixed layer depths (MLD) [46,47,52,54,55]. Ref. [56] refined the approach by using SST and SSH data. This required capturing two baroclinic modes and producing accurate velocity estimates down to a depth of around 1000 m. Using a single hybrid baroclinic mode, referred to as a 'surface mode', the method was simplified in [57–60]. It is worth mentioning that the SQG approach not only is able to reconstruct subsurface horizontal velocities from a single snapshot of SST or SSH but also upper ocean dynamics [46,61–63]. Another effective method to simulate three-dimensional (3D) ocean dynamics is to include in-situ and satellite measurements in high-resolution numerical models [64]. The results of data assimilation are certainly impacted by particular model configurations, which are significant sources of uncertainty, even though data assimilation is unquestionably essential to obtaining realistic projections and analysis. SQG, on the other hand, is a simplified diagnostic model that can be applied only using observations and allows for the retrieval of 3D ocean currents using the knowledge of surface information from remote sensing and an estimation of the vertical density. The SQG technique requires substantially less computer power and is not affected by specific model setups and uncertainties.

In this work, we explored the challenge of using SQG in the Arctic Ocean for the first time. We assessed the capability of SQG to reconstruct the three-dimensional (3D)

horizontal ocean currents in four different Arctic seas: Nordic, Barents, East Siberian, and Beaufort. The paper is organized as follows: Section 2 provides information about the data used in this study, and Section 3 describes the methodology applied. Section 4 presents (a) the results of applying the effective SQG approach using surface TOPAZ4 reanalysis information and validating the reconstructions with TOPAZ4 geostrophic and total currents at each depth and (b) the application of the SQG approach to the remotely sensed Sea Level Anomaly product using the stratification information from in-situ EN4 data and validating the reconstructions using geostrophic velocities from in-situ EN4 data. Section 5 summarizes the main results and final conclusions.

2. Data

2.1. Reanalysis Data

The TOPAZ4 system was developed at the Nansen Environmental and Remote Sensing Center and is run operationally at the Meteorological Institute of Norway. The operational TOPAZ4 Arctic Ocean system is a coupled ice–ocean data assimilation system that uses the HYCOM-CICE model at a resolution of 10 km over the whole Arctic and the Ensemble Kalman Filter (EnKF) running 100 dynamical members to jointly assimilate all available ocean and sea ice observations jointly [65]. The atmospheric forcing fields are from the ECMWF. The HYCOM-CICE model is run daily to provide 10 days of forecasts (average of 10 members) of the 3D physical ocean variables, including sea ice. Data assimilation is performed weekly to provide 7 days of analysis (ensemble average). The output products are interpolated on a grid of 12.5 km resolution at the North Pole (equivalent to 1/8 deg in mid-latitudes) on a polar stereographic projection and hybrid vertical layers are interpolated to 12 fixed levels. The system provides both the near real-time forecast and reanalysis products of the Copernicus Marine Services Arctic Monitoring and Forecasting Center (Arctic MFC). Near-real-time daily outputs from TOPAZ4 for the year 2018 for the first 8 vertical levels (surface, 30, 50, 100, 200, 400, 700, and 1000 m) are used in this study.

2.2. Remotely Sensed Data

We use the experimental AVISO Sea Level Anomalies (cm) for Arctic Ocean (V1.2) gridded multimission altimeter products [66]. This is an optimally interpolated product, especially tailored to the Arctic Ocean, that merges three different altimeter missions: SARAL/AltiKa, CryoSat-2, and Sentinel-3A. The multi-mission sea level heights are computed with respect to a twenty-year mean. This product was processed by SSALTO/DUACS (DOI 10.24400/527896/a01-2020.001) and distributed by AVISO+ (https://www.aviso.altimetry.fr (accessed on 12 February 2023)) with support from CNES.

2.3. In-Situ Data

The Met Office Hadley Center global objective analysis product's most recent version 4.2.1 (EN4) has provided monthly ocean temperature and salinity profiles with objective analyses and uncertainty estimates since 1900 [67]. EN4 salinity data rely on observations from Argo floats, Arctic Synoptic Basin-Wide Oceanography, the Global Temperature and Salinity Profile program, and the World Ocean Database. Salinity profiles are available on a uniform 1º horizontal resolution grid with 42 depth levels. We use the first 26 layers, whose depths are 5, 15, 25, 35, 45, 56, 66, 77, 87, 98, 110, 122, 135, 149, 166, 185, 207, 235, 271, 315, 373, 447, 541, 657, 800, and 968 m.

3. Methods

3.1. Surface Quasi-Geostrophic Approach

Refs. [46,47] suggested that an effective version of the Surface Quasi-Geostrophic equations could be used to predict the mesoscale and submesoscale dynamics of the upper ocean layers. They used the potential vorticity (PV) principle of invertibility, which allows the diagnosis of the three-dimensional (3D) dynamics of a balanced flow from knowledge of PV in the interior of the ocean and density on the vertical boundaries [68]. If we make

the assumption that the flow is in quasi-geostrophic equilibrium, the problem consists of inverting the equation

$$\nabla^2\psi + \frac{\partial}{\partial z}\left(\frac{f_0^2}{N^2}\frac{\partial\psi}{\partial z}\right) = Q, \tag{1}$$

where $\nabla = (\partial x, \partial y)$, ψ is the stream function of the flow, f_0 is the local Coriolis frequency, $N(z)$ is the Brunt–Väisälä frequency, and Q is the PV anomaly. To relate the stream function to buoyancy, the boundary conditions can be derived from the hydrostatic equation. They may be described as follows for the ocean surface:

$$f_0\frac{\partial\psi}{\partial z}|_s = b_s, \tag{2}$$

where b_s is the surface buoyancy. The surface buoyancy field b_s is proportional to the density anomaly ρ':

$$b_s(\vec{x}) = -g\frac{\rho'(\vec{x})}{\rho_0}, \tag{3}$$

where ρ_0 is the mean density inside each study area. We estimate the density anomaly ρ' by combining the sea surface temperature (SST) and sea surface salinity (SSS) [69]. We use the squared Brunt–Väisäla frequency, N^2, to account for the stratification strength within the water column, which is calculated using density differences between depth levels ($N^2 = -(g/\rho_0)\delta\rho(z)/\delta z$).

The solution to the PV inversion problem (Equations (1) and (2)) can be written in terms of a transfer function [48,70]:

$$\hat{\psi}_b(\vec{k}, z) = F(\vec{k}, z)b_s(\vec{k}), \tag{4}$$

where the hat stands for the Fourier transform, $k = (k_x, k_y)$ is the horizontal wave vector, and $F(\vec{k}, z)$ is a transfer function that depends on the modulus of the wavevector and the depth z. The reconstruction of the stream function $\psi(\vec{x}, z)$ from surface buoyancy b_s, e.g., from satellite measurements of SST and SSS, is done using the following transfer function [71]:

$$F(\vec{k}, z) = \frac{1}{n_0 f_0 k}\exp(n_0 k z). \tag{5}$$

where n_0 is the Prandtl ratio [72], which is related to stratification through $N(z) = n_0 f_0$. This means that the SQG approach allows us to derive the stream function at each depth using an exponentially decaying function that depends on the water column stratification.

The stream function $\psi(\vec{x}, z)$ can also be similarly derived from the surface stream function $\psi_s(\vec{x})$), e.g., from satellite measurements of SSH:

$$\hat{\psi}_\eta(\vec{k}, z) = G(\vec{k}, z)\psi_s(\vec{k}), \tag{6}$$

where the surface stream function $\psi_s(\vec{x})$ is obtained from the SSH $\eta(\vec{x})$ following the geostrophic relation [73] through

$$\psi_s(\vec{x}) = \frac{g}{f_0}\eta(\vec{x}), \tag{7}$$

and using the transfer function G as in [48,54]:

$$G(\vec{k}, z) = \exp(n_0 k z). \tag{8}$$

From the stream function $\psi_\eta(\vec{x},z)$ and $\psi_b(\vec{x},z)$, we can directly retrieve horizontal velocities $\vec{v}_\eta$ and $\vec{v}_b$ at each depth:

$$\begin{aligned} u(\vec{x},z) &= -\frac{\partial\psi(\vec{x},z)}{\partial y}; \\ v(\vec{x},z) &= \frac{\partial\psi(\vec{x},z)}{\partial x}. \end{aligned} \tag{9}$$

Finally, we can also retrieve the horizontal velocities at each depth from the sea surface velocities (SSV) obtained using the following:

$$\hat{v}_v(\vec{k},z) = \exp(n_0 kz)\hat{v}_s(\vec{k}). \tag{10}$$

We evaluate the three different reconstructions with geostrophic velocities. The geostrophic velocities at each depth are computed by subtracting the thermal wind component at each depth from the surface geostrophic velocities:

$$\begin{aligned} u_g(\vec{x},z) &= u_g(\vec{x},z=0) - u_t(\vec{x},z); \\ v_g(\vec{x},z) &= v_g(\vec{x},z=0) - v_t(\vec{x},z), \end{aligned} \tag{11}$$

where the surface geostrophic velocities were retrieved using

$$u_g(\vec{x},z=0) = -\frac{\partial\psi_s(\vec{x})}{\partial y}; v_g(\vec{x},z=0) = \frac{\partial\psi_s(\vec{x})}{\partial x}, \tag{12}$$

and the thermal wind contribution at each depth is retrieved using equations [73]

$$u_t(\vec{x},z) = \frac{1}{\rho_0 g f_0}\frac{\partial\rho(\vec{x},z)}{\partial y}; v_t(\vec{x},z) = \frac{1}{\rho_0 g f_0} - \frac{\partial\rho(\vec{x},z)}{\partial x}. \tag{13}$$

The vertical component of relative vorticity $\zeta(\vec{x},z)$, from the different velocity reconstructions, is also examined:

$$\zeta(\vec{x},z) = \frac{\partial v}{\partial x} - \frac{\partial u}{\partial y}. \tag{14}$$

Using the relative vorticity, the potential vorticity (PV) is computed as follows:

$$PV(\vec{x},z) = \zeta(\vec{x},z) - \frac{\partial(\frac{bf_0}{N^2})}{\partial z}. \tag{15}$$

3.2. Application to Reanalysis Data

We apply the SQG approach to assess three different reconstructions of the ocean currents in the upper layers of the ocean using information from the TOPAZ4 system: (a) reconstruction from SSH $\vec{v}_\eta$ (Equations (6) and (7)), (b) reconstruction from SSB $\vec{v}_b$ (Equations (4) and (5)), and (c) reconstruction from surface velocities $\vec{v}_{vel}$ (Equation (10)). We reconstruct the ocean currents from surface information in the first 8 layers of the TOPAZ4 reanalysis (0, 30, 50, 100, 200, 400, 700, and 1000 m). To apply the SQG relation, we have high-pass-filtered the TOPAZ4 outputs as SQG relations are valid for the mesoscale structures. We use a Gaussian filter to remove scales greater than 350 km to the TOPAZ4 SST, SSS, SSH, $\vec{u}$, and $\vec{v}$. We compute the density and buoyancy following Equation (3) and the Thermodynamic Equation of Seawater (TEOS-10) [69]. We are interested in analyzing the ability to reconstruct the ocean current directions using three different inputs, so we normalize the resulting reconstructed currents by the root mean square (RMS) at each depth. The amplitude of the currents could be adjusted by adding an additional parameter to the SQG equations—for example, using the kinetic energy has been proven to give reasonable results [54].

We reconstructed the 3D ocean dynamics during the year 2018 using daily outputs of the TOPAZ4 system in four areas. The areas of study are defined as follows: the Nordic Seas [70–80°N, 20°W–15°E], the Barents Sea [70–80°N, 20–60°E], the East Siberian Sea [70–80°N, 140–180°E], and the Beaufort Sea [70–80°N, 170°W–130°W] (black boxes in Figure 1). To apply the Surface Quasi-Geostrophic (SQG) approach, we need to compute the Prandtl ratio, which depends on the stratification, defined as the Brunt-Väisälä frequency (Section 3.1).

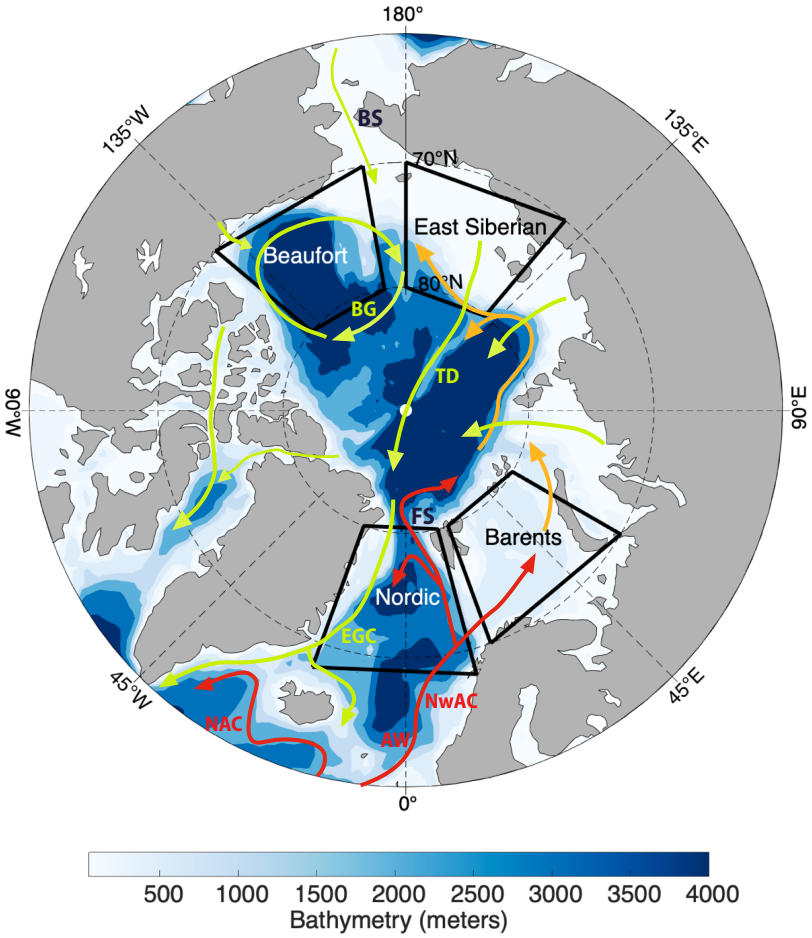

Figure 1. Ocean bottom bathymetry with a schematic of main ocean circulation adapted from [74] (Atlantic water (AW) circulation is shown in red/orange arrows and the freshwater circulation is shown in green arrows). The four study areas are highlighted in black rectangles: the Nordic Seas [70–80°N, 20°W–15°E], the Barents Sea [70–80°N, 20–60°E], the East Siberian Sea [70–80°N, 140–180°E], and the Beaufort Sea [70–80°N, 170°W–130°W]. Specific features and currents are mentioned in the text with the following abbreviations: BS = Bering Strait, BG = Beaufort Gyre, TD = Transpolar Drift, FS = Fram Strait, EGC = East Greenland Current, NAC = North Atlantic Current; NwAC = Norwegian Atlantic Current.

3.3. Application to Remotely Sensed SLA Data

We apply the SQG approach to reconstruct the 3D dynamics, using as input a remotely sensed Sea Level Anomaly (SLA) Arctic product. The product merges data from the SARAL/AltiKa, Cryosat-2, and Sentinel-3A satellites over 4 days on a 25 km Equal-Area Scalable Earth (EASE) grid adapted to polar areas. To apply the SQG approach, we interpolate the product into a regular grid of 0.25 degrees. We reconstruct the 3D ocean currents in the four study areas detailed in Section 3.2 (Figure 1), in the first 1000 m. We use the first 26 layers of the EN4 product (Section 2.3). Ocean currents are normalized in the same way as in Section 3.2.

4. Results and Discussion

4.1. SQG Assessment Using Reanalysis Data

The mean monthly profiles of density and Brunt–Väisälä frequency (Figure 2) exhibit a clear seasonal variation in the water column stratification in the Nordic and Barents Seas. In comparison, the seasonal variation is less clear in the East Siberian and Beaufort Seas. For all four regions, months from July to October exhibit higher stratification (higher N^2), with maximum peaks in August and September, which is associated with freshwater inflows from ice melting, river discharge peaks, and warmer temperatures due to higher atmospheric heat fluxes into the ocean in summer. In the late spring–summer months (June, July, August, and September), the surface accumulates all the freshwater inputs and the water column is deeply stratified. From September, and associated with the increased passage of storms during autumn, the water column starts to mix progressively in October, November, and December. Ocean mixing causes lower stratification (lower N^2) in the winter and spring months (January, February, March, April, and May). In the Nordic Seas (Figure 2a,b), the surface reaches the minimum mean densities in August (26.4 kg/m^3) and maximum surface densities (27.3 kg/m^3) in April. The summer and fall profiles depict a surface mixed layer and a clear pycnocline (high-density gradient) located immediately below it in the first 100 m with an associated maximum in N^2. The density reaches 27.7 kg/m^3 at 200 m, and at deeper depths, it is relatively constant over the year, whereas the N^2 is close to zero. The Barents Sea (Figure 2c,d) is found to have higher surface density means in the winter and spring months, reaching a maximum in March (27.5 kg/m^3). The water column is well mixed in the winter and spring months. Note that in the Barents Sea, the sigma values are only up to 400 m; therefore, N^2 can only be calculated down to the previous vertical level (i.e., 200 m depth), as differences in density between consecutive depth levels are used to compute the stratification.

The East Siberian Sea (see Figure 2e,f) is characterized by a more stable, highly stratified water column throughout the year in the reanalysis data, with a less dense layer on the surface (22.8–23.8 kg/m^3), associated with cold and low-salinity waters, a pronounced pycnocline, and the denser Atlantic water (higher-salinity), with densities higher than 27.6 kg/m^3 below 150–200 m [4]. Riverine discharge has a great influence on the East Siberian Sea, and we would expect the density and stratification profiles to present a stronger seasonal variability than the reanalysis data reproduce, as the river discharge and advection processes are seasonal. Moreover, the reanalysis data do not seem to reproduce the winter deep convection that forms the Arctic halocline waters. The East Siberian waters present the highest stratification of the four regions (three times higher), with a maximum of around 7×10^{-4} s^{-2} at 30 m depth. This stratification strengthening might be explained by the very low salinity from Russian rivers trapped in the surface layer (around 50 m). Minimum density (22.8 kg/m^3) is reached at surface waters in August and maximum densities (23.8 kg/m^3) in April, resembling the seasonality in the riverine discharges. At 200 m, the density is relatively stable at 27.6 kg/m^3 during the whole year, probably representing the Atlantic layer [75]. The surface waters of the Beaufort Sea (Figure 2g,h) present a higher range of density variability, with a minimum density (23.9 kg/m^3) in September and maximum densities (24.6 kg/m^3) in April. The upper layer (<200 m depth) within the Beaufort Sea holds the lowest-density waters of the four studied regions. One explanation for this feature relies on the anticyclonic circulation regime, which tends to accumulate the freshwater from sea ice melting during the melt season (June–October) and store it during the rest of the year. Moreover, the Beaufort Sea receives freshwater from the Russian side and Pacific waters through the Bering Strait (BS in Figure 1), which have relatively low salinity due to the influence of the Yukon, which also contributes to the lower salinity observed within the upper layer of the Beaufort waters [19]. In contrast to the other three regions, where stratification becomes null below a 200 m depth, likely driven by small changes in the temperature [75], stratification in the Beaufort Sea extends down to a 400 m depth, coinciding with the base of the dome associated with the anticyclonic Beaufort Gyre [10].

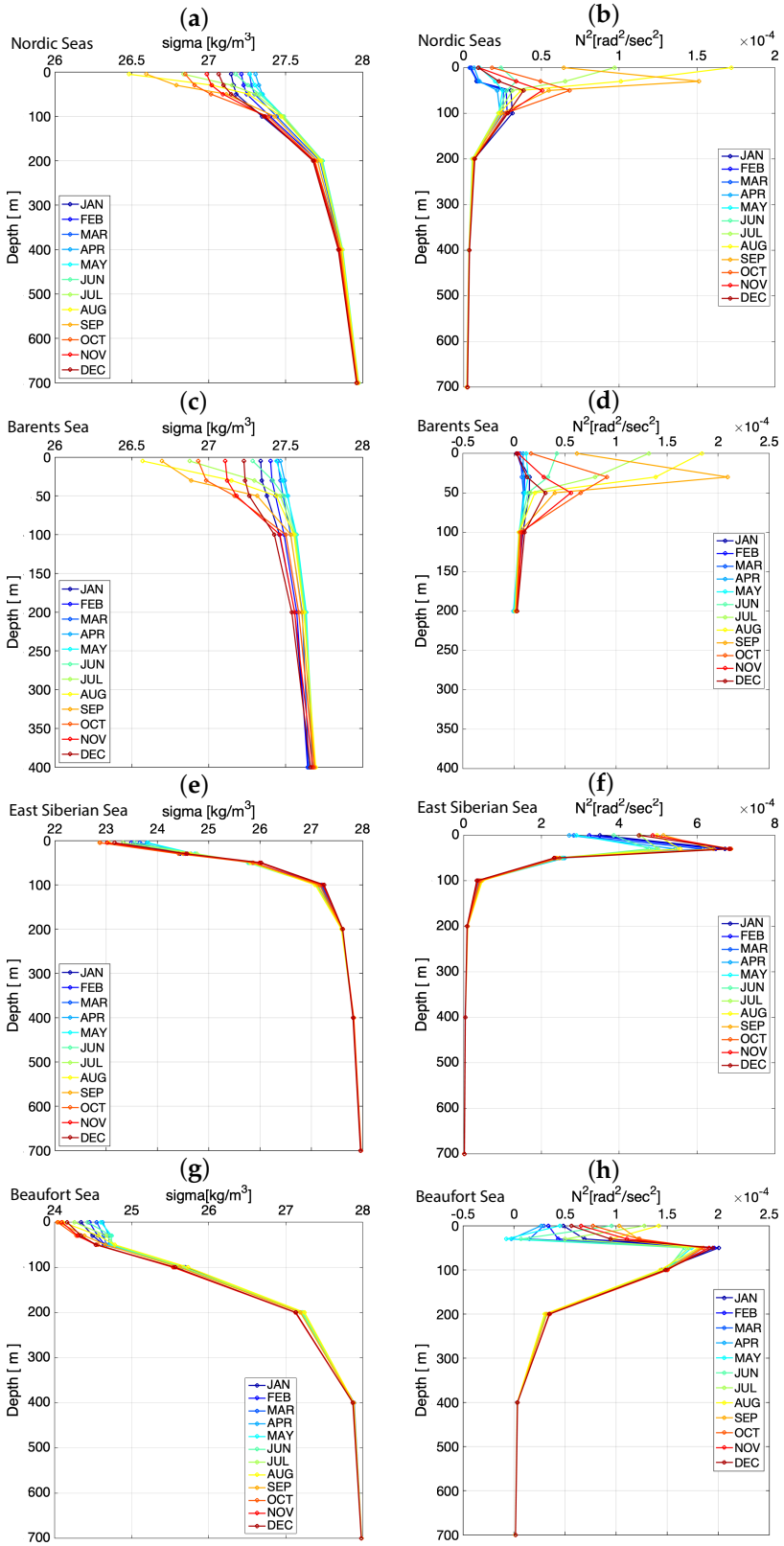

Figure 2. TOPAZ 4 mean monthly profiles of density and squared Brunt–Väisälä frequency in the (**a**,**b**) Nordic Seas, (**c**,**d**) Barents Sea, (**e**,**f**) East Siberian Sea, and (**g**,**h**) Beaufort Sea. Note that, in order to properly capture seasonal variations, axis limits differ among panels.

We computed the daily mean Prandtl ratio (n_0) for each area, as the mean Brunt–Väisälä frequency in the first 100 m divided by the mean Coriolis frequency in the area. Mean

n_0 values for each season can be found in Table 1. The Coriolis frequency f_0 was fixed to the value corresponding to the mean latitude of the area; for example, in the Nordic Seas, f_0 is 1.405 $\times$ 10^{-4} s^{-1}, which corresponds to a latitude of 74.95°N, and in the Beaufort Sea, the f_0 is 1.4195 $\times$ 10^{-4} s^{-1}, which corresponds to a latitude of 77.45°N. As a first approach, we assume a constant Prandtl ratio through the water column. This assumption is less accurate in spring and summer months as the water column is highly stratified, and therefore surface structures are less correlated with depth, and more realistic during winter months when the upper layers of the water column are mixed (Figure 2). A depth-varying Prandtl ratio [56] would lead to better reconstructions in the water column. However, we would also need a higher-resolution model to be able to improve the 3D reconstruction by assuming a non-constant Prandtl ratio, which is not within the scope of this study, as we wish to apply the approach to the resolution of remote sensing data. Given the slight variations in f_0 for the different regions, the n_0 values in Table 1 are fairly representative of the stratification strength. From these values, we expect that the surface structures in the Nordic and Barents Seas will easily propagate downwards through the water column, whereas they will be retained at shallower depths in the Beaufort and East Siberian Seas.

Table 1. Seasonal and yearly means of the Prandtl ratio n_0 within the study areas for the year 2018 using TOPAZ4 reanalysis.

	Winter	Spring	Summer	Autumn	Year Mean
Nordic Seas	28.15	32.14	57.67	39.27	39.38
Barents Sea	20.36	25.57	54.77	33.35	33.61
East Siberian Sea	119.20	114.57	124.89	127.19	121.50
Beaufort Sea	69.08	63.51	83.17	80.65	74.16

An example of the surface currents reconstructed from SSH and SSB for 28 August and 28 February (2018) in the Nordic Seas (Figure 3) shows that reconstruction from SSB is not able to see key mesoscale surface currents seen in SSH in the Nordic Seas. Note that surface currents are non-dimensional as they are normalized by their RMS (see Section 3.2). Similar results are found both for summer and winter examples. Looking more closely at the features represented in Figure 3, we can distinguish a southwest current close to the Central–East Greenland coast (South of Kangertittivaq Bay) in both reconstructions from SSH and SSV (structure 1 in Figure 3). Although present independently of the season, this coastal current intensifies in winter (28 February), and is likely confined by sea ice growth. This coastal current seems unrealistic for the SSB approach, appearing only in wintertime and widely distributed along the East Greenland coast. An anticyclonic mesoscale eddy located at ∼70ºN and ∼3ºE (structure 2 in Figure 3) is observed on both SSH and SSV reconstructions (Figure 3a,c) and missing on the SSB one (Figure 3b). This is the quasi-permanent anticyclonic eddy known as the Lofoten vortex [76], located in the center of the Lofoten Basin. The Lofoten vortex seems to be maintained partly (∼43%) by the merging of eddies shed from the boundary current along the Norwegian continental slope [76,77], and partly by winter convection associated with local heat loss [78,79]. Nevertheless, recent studies based on numerical simulations suggest that wintertime convection would mainly serve to vertically homogenize and densify the vortex, indicating that the repeated merging events would be the primary mechanism of the Lofoten vortex's regeneration [80].

Although present in both summer and winter [81], there is a clear summer strengthening that leads to a smoother and smaller anticyclonic mesoscale eddy off the west coast of Svalbard, at the easternmost part of the Fram Strait section (∼77.5ºN, ∼8ºE) (structure 3 in Figure 3a,c).

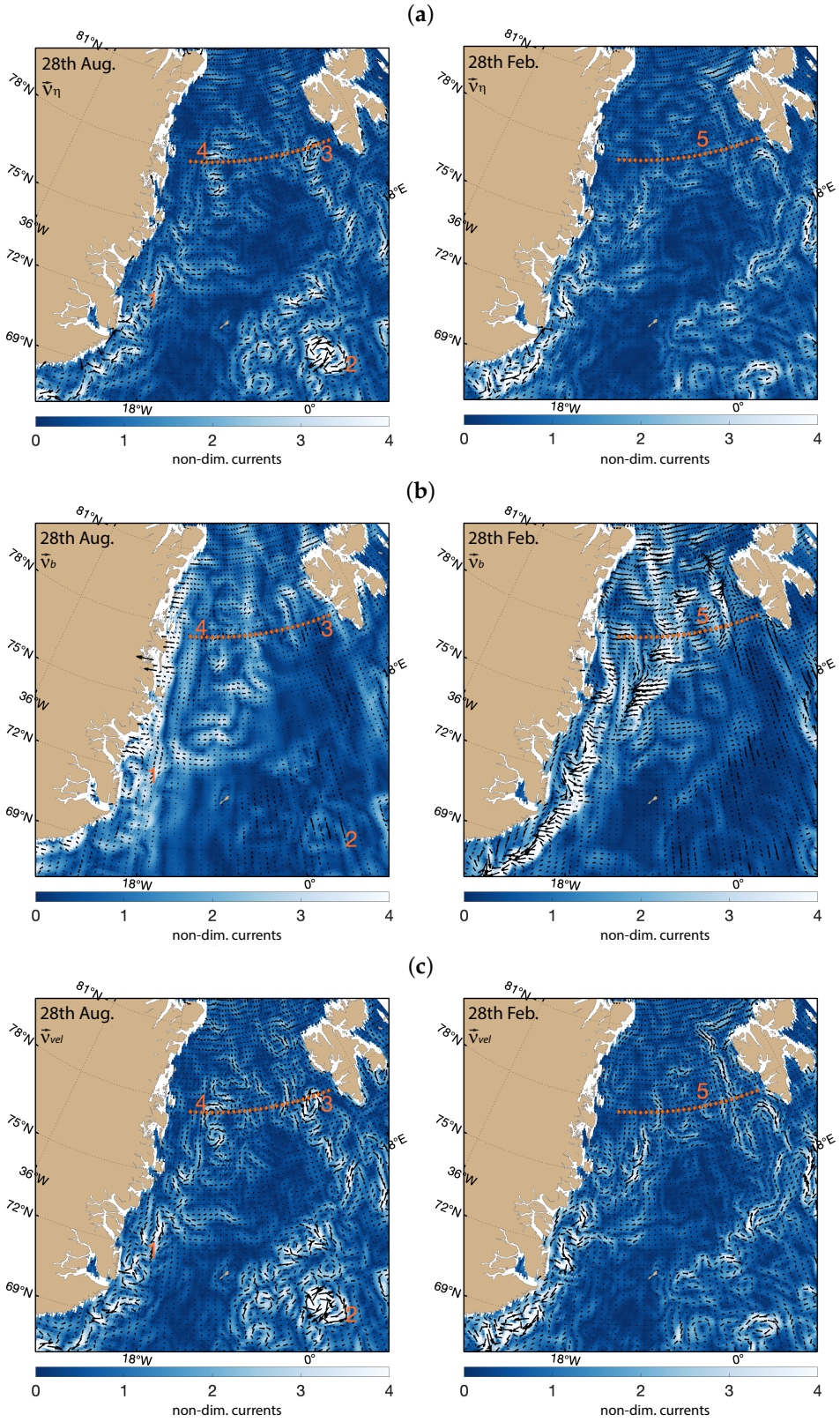

Figure 3. Example of normalized surface currents for 28 August (**left**) and 28 February (**right**) 2018 in Nordic Seas. (**a**) Reconstruction from SSH $\vec{v}_\eta$, (**b**) reconstruction from SSB $\vec{v}_b$, (**c**) reconstruction from surface velocities (SSV) $\vec{v}_{vel}$. Fram Strait (FS) section at latitude 77.5°N in red diamonds. Red numbers indicate the mesoscale structures described and discussed in the main text: southwest current (1), anticyclonic eddies (2,3), and cyclonic eddies (4,5).

In contrast to the two anticyclonic eddies already described, there is a summer cyclonic mesoscale eddy (structure 4 in Figure 3) located at the westernmost region of the Fram Strait section (∼77.5ºN, ∼12ºW). Its location suggests that this cyclonic eddy is part of the East Greenland Current (EGC in Figure 1) (associated with the NE-Greenland continental slope). In winter, there is also a cyclonic eddy located in the eastern region of the Fram Strait (∼77.5ºN, ∼6ºE, structure 5 in Figure 3) [82]. The reanalysis temperature and salinity data used to compute the SSB do not exhibit the same dynamical patterns as the SSH, or they are unable to resolve the significant freshwater influence in this region, which may explain why none of the eddies can be identified in the SSB reconstruction. Nevertheless, the in-depth propagation of these two eddies located along the Fram Strait (the anticyclonic and the cyclonic ones), along with other features, are studied for the three different SQG reconstructions within z-x transects.

Summer and winter sections (Figures 4 and 5, respectively) along the Fram Strait (latitude = 77.5ºN) allow us to compare the ocean 3D dynamics reconstructed from the (a) surface height, (b) surface buoyancy, and (c) surface velocities, and compare them to (d) geostrophic TOPAZ4 velocities and (e) total TOPAZ4 velocities. Considering the total TOPAZ4 velocities as reasonably representative of the real circulation, we can see in both the summer and winter scenarios (Figures 4 and 5, respectively), that the total TOPAZ4 velocities contain a baroclinicity that is not reproduced in the geostrophic TOPAZ4. Reconstructing 3D dynamics from SSH and SSV performs closely to the geostrophic TOPAZ velocities, essentially barotropic, compared to the reconstruction that is achieved from SSB. As expected from the relatively low n_0 values obtained for the Nordic Seas (Table 1) in summer, the most important features observed at the surface are propagated downwards through the water column. This is the case of the mesoscale anticyclonic eddy located at 8ºE in the Fram Strait (structure 3 in Figures 3 and 4), in which the vertical structure is reproduced in the total and geostrophic TOPAZ4 velocities (Figure 4d,e), as well as in the SSH and SSV reconstructions (Figure 4a,b). However, in summer, we can see that the mesoscale cyclonic eddy centered at ∼12ºW (structure 4 in Figures 3 and 4) propagates no deeper than 100 m depth on the total TOPAZ4 velocities, whereas the influence of this eddy on the SSH and SSV reconstructions, as well as on the geostrophic TOPAZ4 velocities, is present down to the sea bottom (∼200 m depth). Given the divergent nature of cyclonic eddies, it is plausible to find the decay of this type of structure at shallower depths than the anticyclonic ones [83]. Moreover, in contrast to the deeper eastern part of the FS section, the wide continental shelf off NE-Greenland would be limiting the vertical extension of the mesoscale eddies at the western side of the FS. Since a constant n_0 value is assumed all over the Nordic Seas at any given depth, and also since the sea bottom effect is not accounted for, none of the reconstructions (or the geostrophic TOPAZ4 velocities) are capable of representing this depth-dependent eddy decay.

In the winter section (Figure 5), there is a cyclonic eddy (structure 5 in Figures 3 and 5) with a surface signature that is moving westward at depth in the total speed (Figure 5e). None of the reconstructions is capable of reproducing this displacement in the vertical. However, assuming the total velocity as the real scenario, the SSH and SSV reconstructions reproduce this surface eddy structure correctly. SSB reconstruction shows this structure further east than it actually is. This result indicate once more that the SSH and SSB from the reanalysis do not exhibit the same dynamical structures, probably indicating that the temperature and salinity do not act as passive tracers of the flow, but they resolve additional phenomena such as the freshwater influence and air–sea interaction.

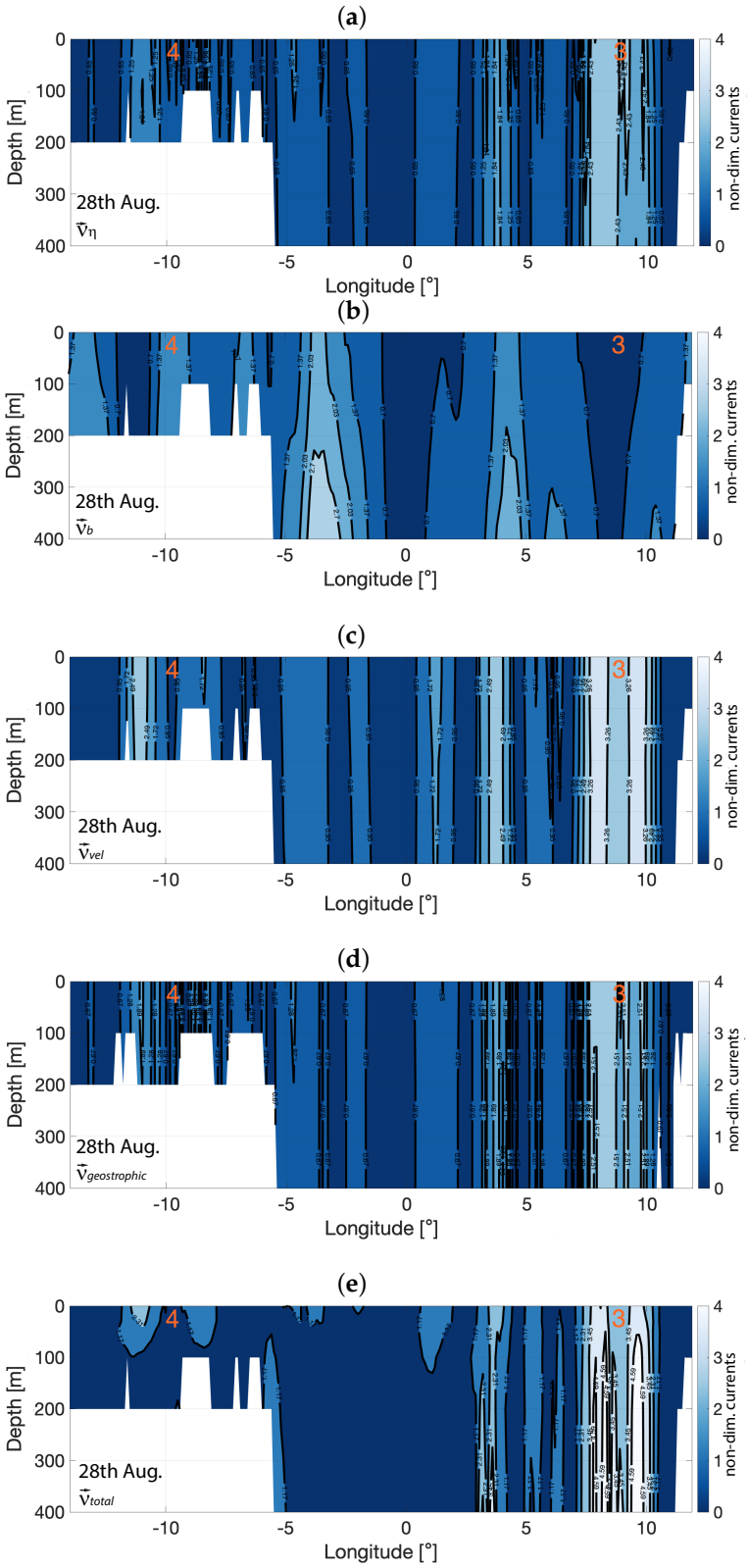

Figure 4. Normalized ocean currents along Fram Strait section (lat = 77.5°N) for 28 August. (**a**) Reconstruction from SSH $\vec{v}_\eta$, (**b**) reconstruction from SSB $\vec{v}_b$, (**c**) reconstruction from SSV $\vec{v}_{vel}$, (**d**) geostrophic TOPAZ4 velocities, (**e**) total TOPAZ4 velocities. Red numbers indicate the mesoscale structures described and discussed in the main text: anticyclonic eddy (3) and cyclonic eddy (4).

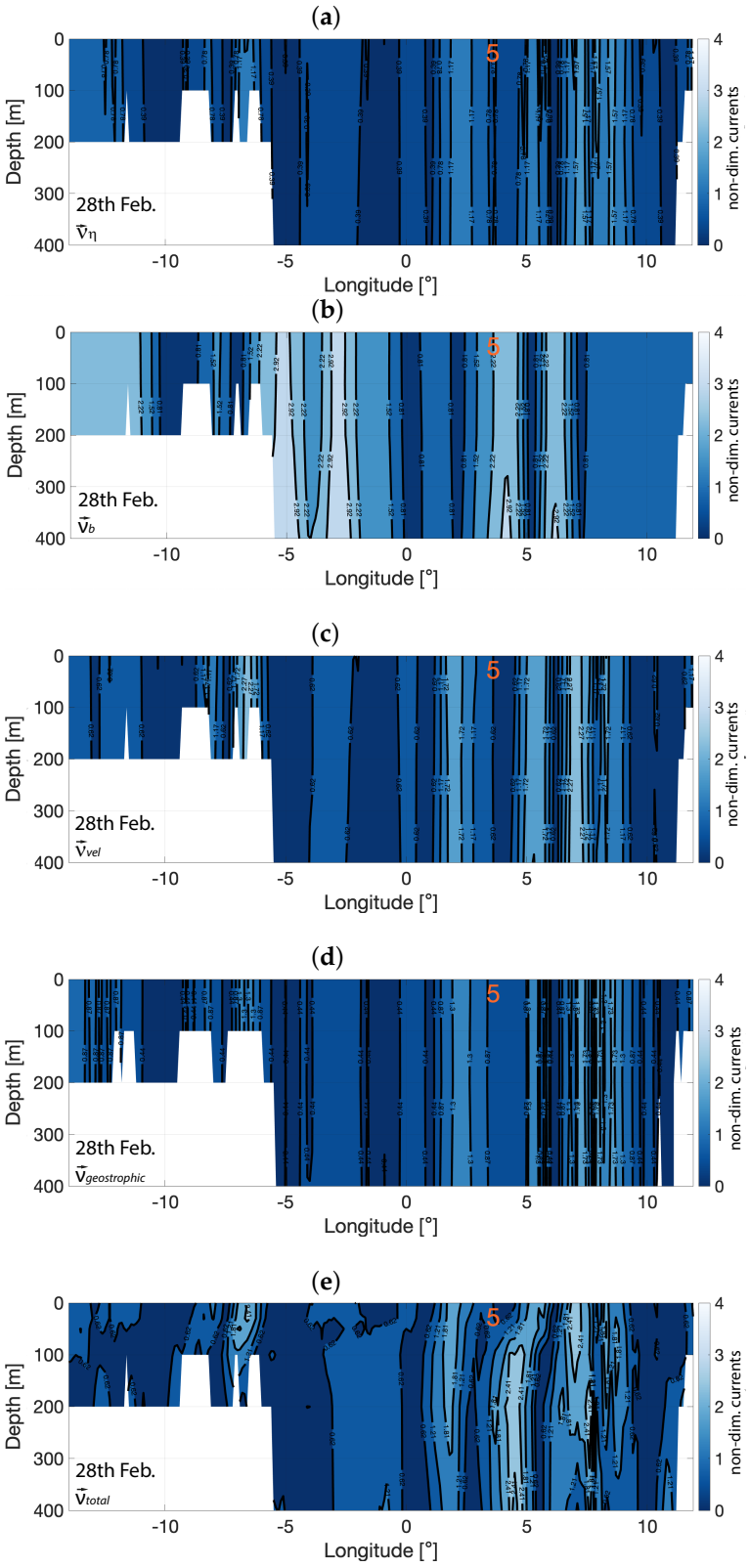

Figure 5. Normalized ocean currents along Fram Strait section (latitude = 77.5°N) for 28 February. (**a**) Reconstruction from SSH ($\vec{v}_\eta$), (**b**) reconstruction from SSB ($\vec{v}_b$), (**c**) reconstruction from SSV ($\vec{v}_{vel}$), (**d**) geostrophic TOPAZ4 velocities, (**e**) total TOPAZ4 velocities. Red numbers indicate the cyclonic eddy (5) described and discussed in the main text.

As for the Nordic Seas, the SSB reconstruction shows less mesoscale circulation structures in the Beaufort Sea (Figure 6) than the SSH and SSV reconstructions. Two features clearly resolved by the SSB approach are the NE surface current of Pacific waters entering the Beaufort Sea along the Alaskan coast (structure 1 in Figure 6), and an undefined but large structure associated with the Mackenzie discharge plume (∼70ºN, ∼135ºW, structure 2 in Figure 6), which can be related to water subduction (negative vertical Ekman pumping) [84]. SSH and SSV reconstructions, however, perform better than SSB, showing several mesoscale structures at finer scales [85]. Although the SSV reconstruction seems to be of higher resolution than the SSH one, both of them show three interesting features apart from the NE surface current (structure 1): (i) a well-defined anticyclonic eddy likely associated with the Mackenzie river discharge (structure 2); (ii) a western boundary current along the continental slope off the Northern Alaska–Canada coast (structure 3); and (iii) another anticyclonic eddy located at ∼72.2ºN, 159ºW (∼300 km north of Peard Bay, Alaska), which might be formed by the confluence of Pacific and Beaufort waters along the Chukchi Plateau (structure 4). We select a transect along longitude 159ºW, within the Beaufort Sea, to analyze the vertical structure of the anticyclonic eddy and the end of the NE surface current (Figure 7).

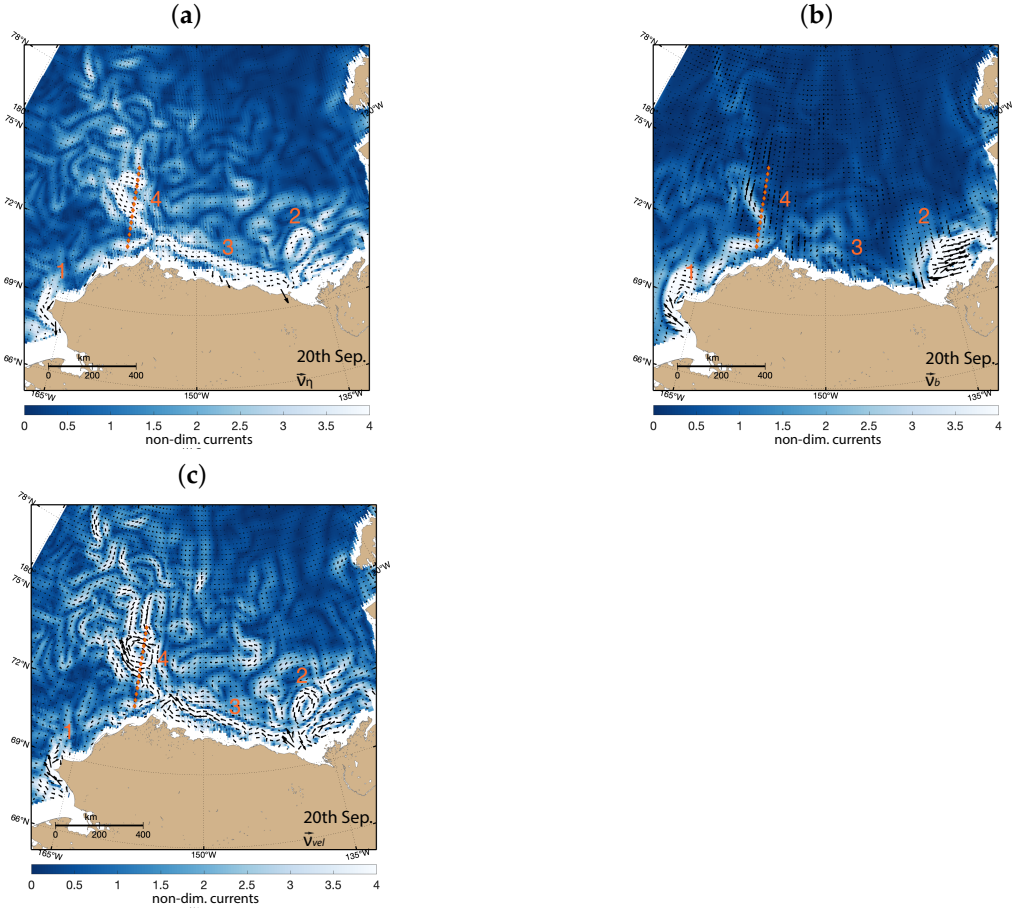

Figure 6. Example of normalized surface currents for 20 September 2018 in the Beaufort Sea. (**a**) Reconstruction from SSH ($\vec{v}_\eta$), (**b**) reconstruction from SSB ($\vec{v}_b$), (**c**) reconstruction from SSV ($\vec{v}_{vel}$). Beaufort Gyre section at longitude 159ºW in red diamonds. Red numbers indicate the mesoscale structures described and discussed in the main text: NE surface current (1), anticyclonic eddies (2,4), and western boundary current (3).

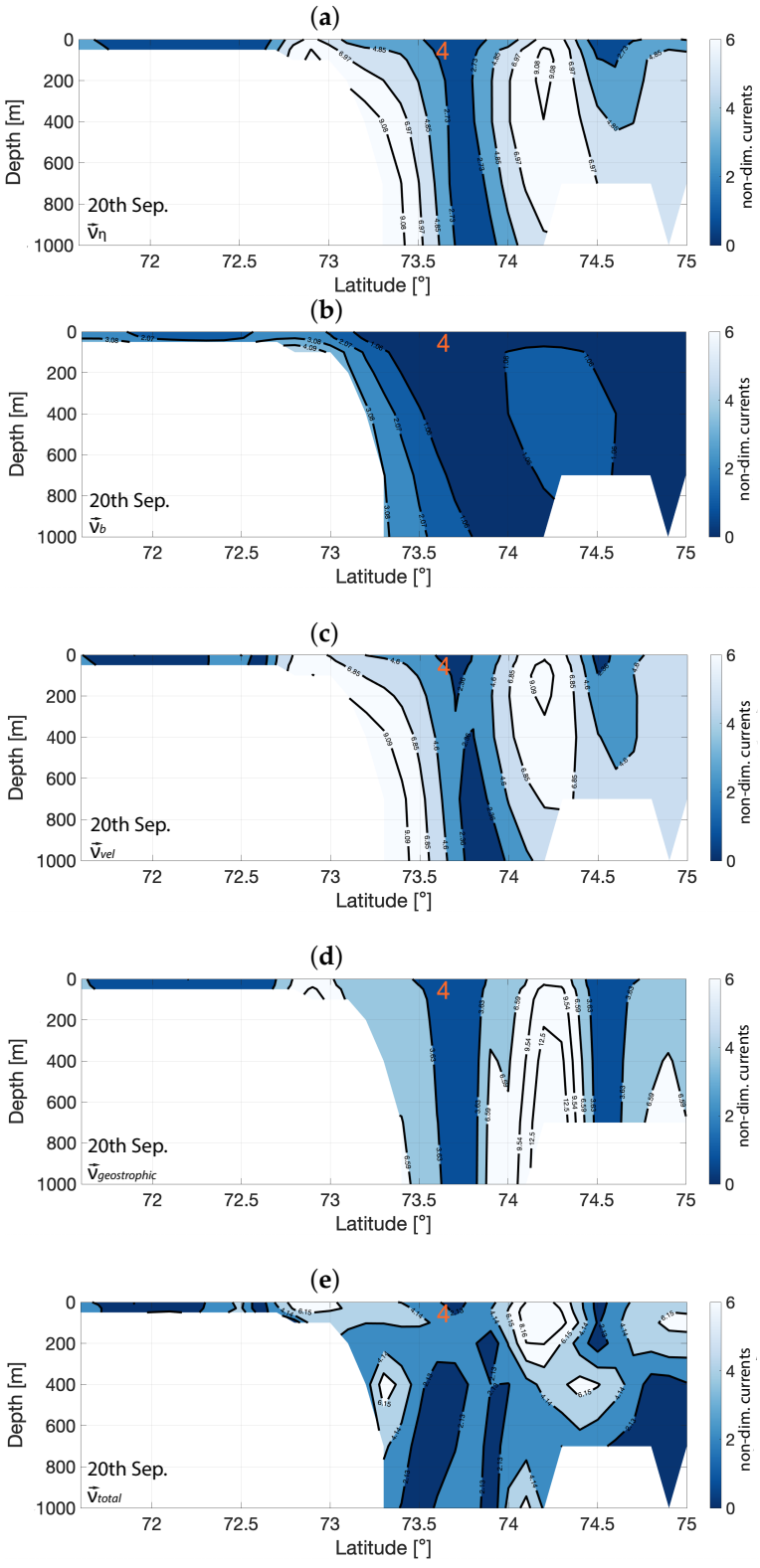

Figure 7. Vertical section of normalized ocean currents along the Beaufort Gyre section (Longitude = 159°W) for 20 September. (**a**) Reconstruction from SSH ($\vec{v}_\eta$), (**b**) reconstruction from SSB ($\vec{v}_b$), (**c**) reconstruction from surface velocities ($\vec{v}_{vel}$), (**d**) geostrophic velocities, (**e**) TOPAZ4 velocities.

Taking the total TOPAZ4 velocities as a reference for the Beaufort Gyre section, our results in the Beaufort Sea show that the vertical reconstructions of SSH and SSV perform better than that of SSB. In-depth propagation is observed for the anticyclonic eddy centered at 73.7ºN (structure 4 in Figures 6 and 7). However, assuming a constant Prandtl ratio leads to a miss-reconstruction of the structures in depth, extrapolating the surface structures deeper than they are in the TOPAZ4 outputs. In the case of the southern branch of the eddy (located above the continental margin, ∼72.8ºN), the total TOPAZ4 velocities show that its vertical propagation remains within the first 80 m depth. However, a continental slope current seems to develop at 400 to 600 m depth. Our reconstructions, however, link both structures, showing the SQG methodology's inability to resolve structures not connected with the surface. The reconstructions propagate the surface signal down to the shelf bottom (100 m depth) and then follow the continental slope to the bottom (1000 m depth). This issue has been assessed in [56] by using a non-constant Prandtl ratio, but one that varies with depth; however, the model resolution that is needed to improve this should also be greater than the one that the TOPAZ4 outputs have.

The inter-comparison of the 3D reconstructions with the geostrophic velocities is synthesized as the mean monthly correlation of relative vorticities at each depth for the year 2018 in Figure 8. To obtain these correlations, for each reconstruction, mean daily relative vorticity profiles in each area and depth are computed and compared with the mean daily relative vorticity profiles of the geostrophic TOPAZ4 currents. Monthly means of these correlation profiles tend to exhibit the best agreement during winter and/or spring months for the four study areas (a: Nordic Seas, b: Barents Sea, c: East Siberian Sea, and d: Beaufort Sea), likely because the water column is less stratified and the Brunt–Väisälä frequency is fairly constant along the water column because of the deep winter convection. For all study areas, the reconstructions from SSB (second column) are not able to reproduce most of the dynamics seen in the geostrophic TOPAZ4 currents, again showing that the spatial surface signatures of SSB are not related to the surface signatures of SSH, related to the geostrophic velocities (Equation (7)). The relative vorticity correlations between the reconstruction from SSH and the model geostrophic current (first column) show good agreement (correlation > 0.8) down to 400 m depth in the Nordic Seas, and to 200 m depth in the Barents and Beaufort Seas. The East Siberian Sea shows a rapid depth-dependent decrease in the correlation between SSH and the TOPAZ4 geostrophic relative vorticities. This correlation obtains values of around 1 at the sea surface, decreases to values <0.6 at 100 m depth, and reaches minimum values of $\sim$0.4 at 400 m depth. The cause of such vertical dissipation of the relative vorticity correlation relies on the strong stratification (N^2 up to 7×10^{-4} s^{-2}) within the upper 100 m of the water column in the East Siberian Seas (Figure 2), which would make this region more challenging in terms of applying the SQG vertical reconstruction approach. It seems that the strong vertical gradient in the surface layer due to the freshwater influence hinders the SQG's reconstruction ability. Another factor that may influence the lower correlation coefficients is that we show an average for a region with much stronger spatial variability. This could also be one of the reasons that we have such disagreement. When the relative vorticities from SSV are compared to those from the geostrophic component (right column), the correlation profile shows mean correlations between 0.6 and 0.8 within the uppermost layers of the four regions (400 m). The lower correlation than in the reconstructions from SSH is likely due to the non-gesotrophic components associated with the atmosphere–ocean interface (e.g., wind stress, atmospheric–ice–ocean interactions) and continental shelf dynamics (e.g., tidal currents). This situation is more pronounced in the East Siberian Sea (correlations < 0.6 except for winter months), where the continental shelf covers most of the region and seems, therefore, to play a crucial role in its own dynamics.

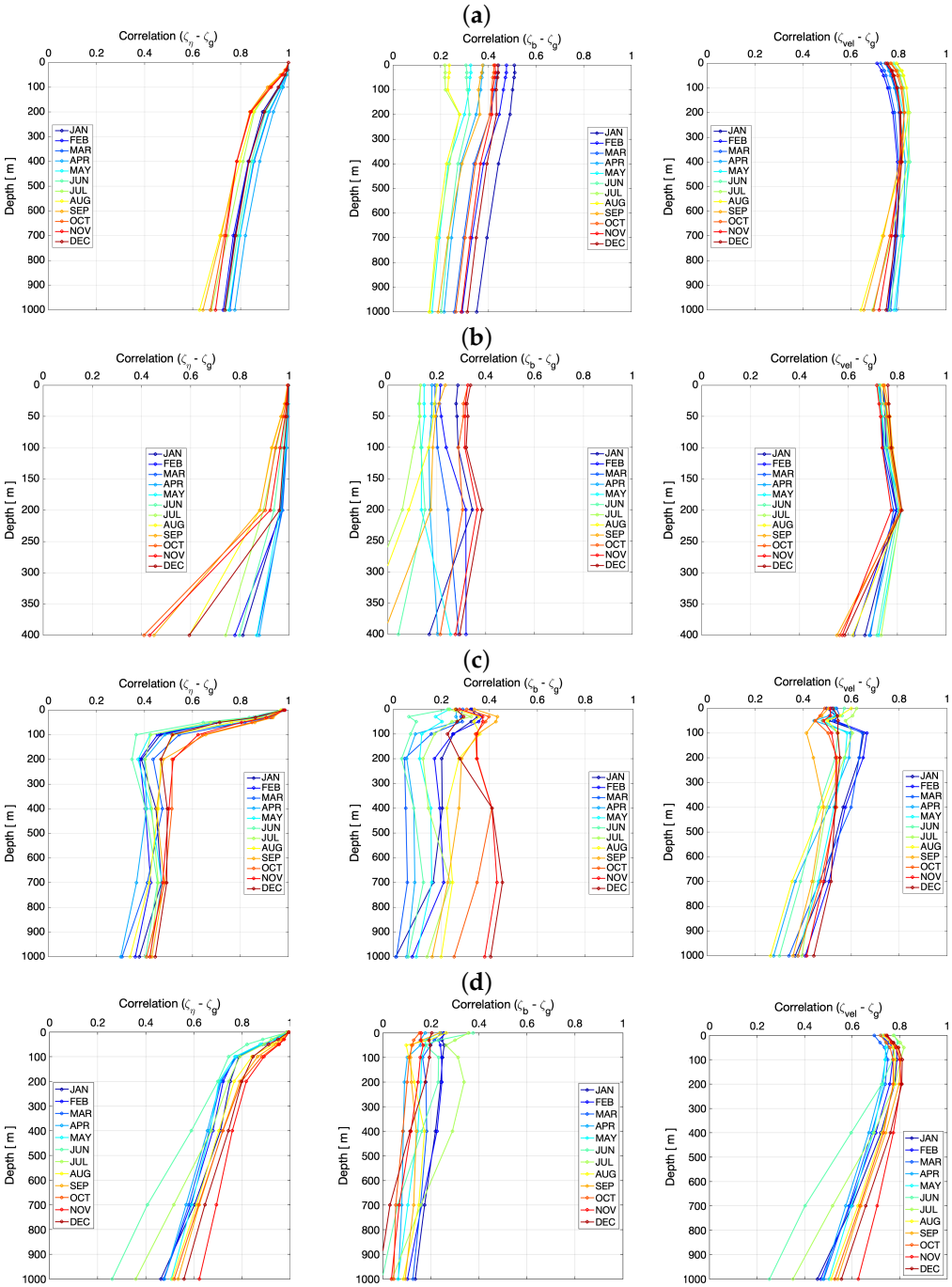

Figure 8. Positive correlations of relative vorticities between (**left**) reconstruction from SSH, (**middle**) reconstruction from SSB, and (**right**) reconstruction from SSV with geostrophic velocities in (**a**) Nordic Seas, (**b**) Barents Sea, (**c**) East Siberian Sea, and (**d**) Beaufort Sea.

In Figure 9, we inter-compare the 3D reconstruction (from SSH $\vec{v}_\eta$, from SSB $\vec{v}_b$, and from SSV $\vec{v}_{vel}$) with the total TOPAZ4 velocities in the form of the mean monthly correlation profiles for each region. We clearly see that the reconstruction from surface buoyancy (second column) fails at reconstructing the total currents in the regions analyzed. Reconstructions from SSH (first column) exhibit a lower correlation when compared to the total currents, showing that only the geostrophic component of the total currents can be reproduced using SSH. Relative vorticity correlations between the reconstruction from SSV and model total currents (third column) exhibit fairly good agreement (correlation > 0.6) up to 200 m. When compared to the total velocities of the model, the 3D reconstruction

degrades quicker as we increase the depth than for the comparison against geostrophic currents (Figure 8), due to the fact that the total velocities include structures that are not reflected in the surface.

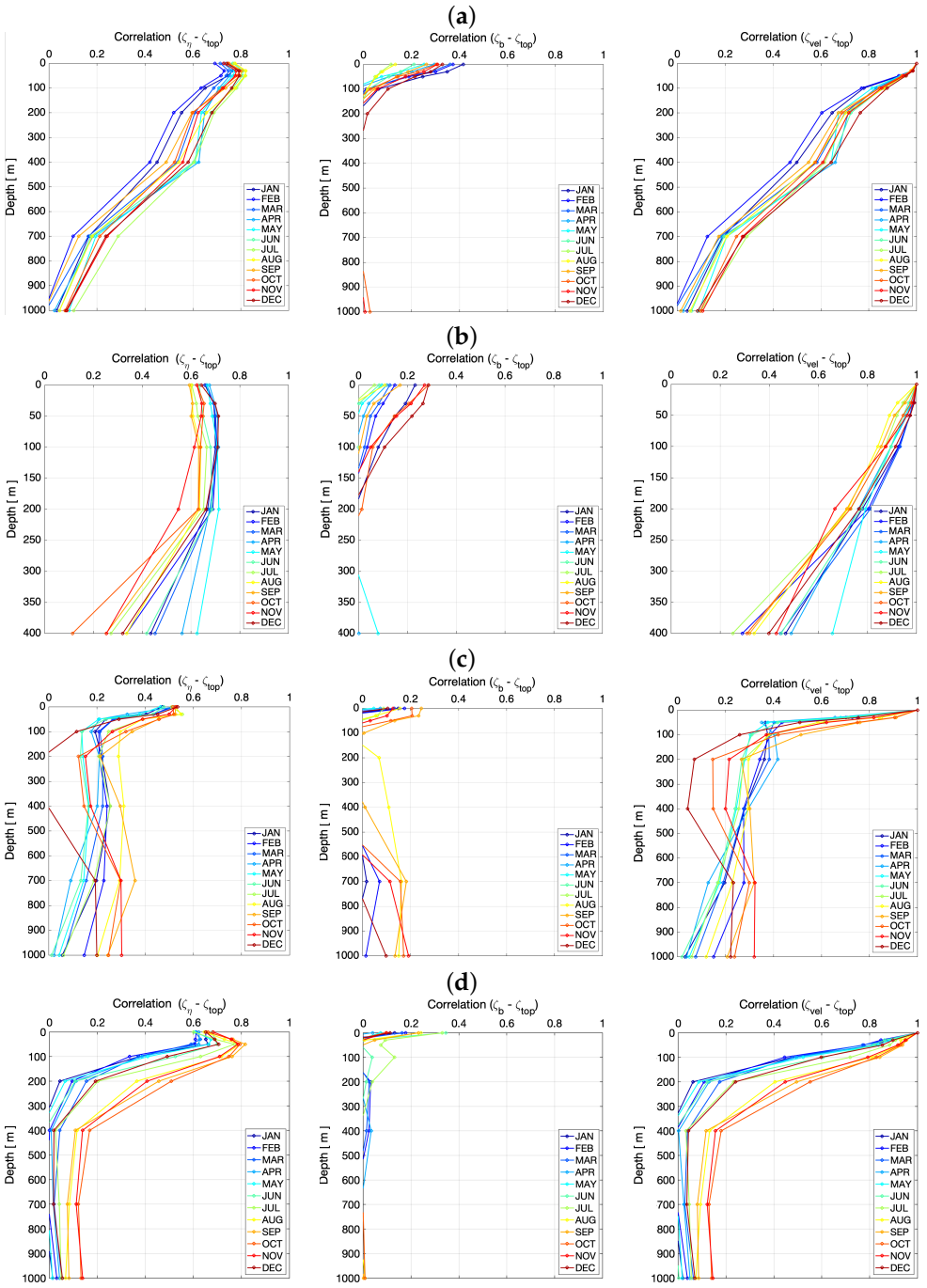

Figure 9. Positive correlations between relative vorticities from TOPAZ4 velocities and (**left**) reconstruction from SSH, (**middle**) reconstruction from SSB, and (**right**) reconstruction from SSV, in (**a**) Nordic Seas, (**b**) Barents Sea, (**c**) East Siberian Sea, and (**d**) Beaufort Sea.

The success of the reconstruction from surface buoyancy mainly depends on the quality of the surface buoyancy as a proxy of the potential vorticity, since the SQG approach assumes that the interior potential vorticity (PV) is spatially correlated with the ocean surface. Ref. [46] showed that the dynamics in the first 500 m can be modeled using effective SGQ equations, assuming that the surface density anomaly represents density anomalies at the base of the mixed layer. Normally, this situation happens after a mixed-

layer deepening period [54]. Figure 10 shows the correlation between the surface buoyancy and the potential vorticity of each layer (dashed line) and the correlation between the sea surface height and the potential vorticity of each layer (solid line). The potential vorticity is calculated using Equation (15) in the four regions analyzed in this study: the Nordic Seas, the Barents Sea, the East Siberian Sea, and the Beaufort Sea (Figure 10a,b,c,d, respectively). The surface buoyancy is only correlated to the potential vorticity up to the first 50 m in the Nordic (Figure 10a) and Barents Seas (Figure 10b), mostly in the winter months. We expect that this is the factor that would hinder the reconstruction of the interior dynamics from the surface buoyancy. Note that, sometimes, the SSH is less correlated to PV than the SSB at more surface layers. This situation happens in the first 50 m in fall and in winter in the Nordic Seas and in the first 100 m in fall and winter in the Barents Sea; in these places and at these times, the correlation results were the best in the SSB reconstructions (Figures 8 and 9). In the East Siberian (Figure 10c) and Beaufort Seas (Figure 10d), the SSH is better correlated with PV than the sea surface buoyancy for the different months of the year.

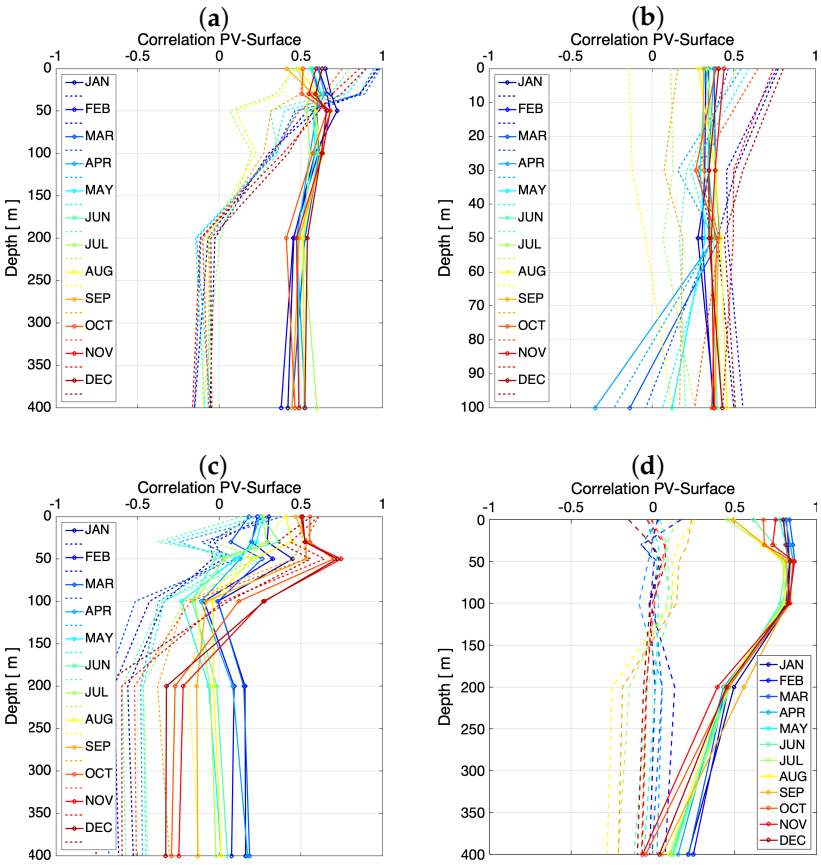

Figure 10. Monthly means of daily correlation in the first 400 m between PV and sea surface height (solid line) and surface buoyancy (dashed line) in the (**a**) Nordic Seas, (**b**) Barents Sea, (**c**) East Siberian Sea, and (**d**) Beaufort Sea.

The performance of SQG using only surface buoyancy as an input contrasts with previous results in the Mediterranean [49]. In the Arctic Seas, it was not possible to infer the 3D dynamics using only the surface temperature and salinity data. Even if the Arctic Seas are strongly influenced by freshwater fluxes and the salinity contribution dominates the density, it seems more plausible to resolve the surface dynamics using buoyancy as a secondary contributor to the sea surface height from altimetry [39,86,87], as opposed to using buoyancy as the only proxy required to resolve the surface dynamics.

The SQG approach has been successfully applied before to more energetic regions, but never to the Arctic Ocean; this is the first time that the SQG is tested in this area. The results are coherent with previous applications, which concluded that the SQG approach is better suited to reconstruct ocean dynamics in the upper 500 m for energetic areas with deep mixed-layer depths [46,47,52,54]. Even if the Arctic region is less energetic, the quality of the reconstructions depends on how mixed/stratified the upper ocean layer is, which partly modulates how the mesoscale structures on the surface are propagated in the water column. The information contained in buoyancy can complement the information on the sea level, but it should not be used as the only input to reconstruct the ocean dynamics. Using SQG, we are able to reconstruct the barotropic component of the flow up to approximately 400 m.

4.2. Reconstruction of 3D Dynamics Using Remotely Sensed Data

We apply the SQG approach to reconstruct the 3D dynamics using as input the remotely sensed Sea Level Anomaly (SLA) data (Section 2.2). We use the information on the in-situ temperature and salinity in the water column provided by the EN4 optimally interpolated product (Section 2.3) to compute the Prandtl ratios. As has been previously described, we compute the monthly Prandtl ratio (n_0) for each area as the mean Brunt–Väisälä frequency within the upper 100 m divided by the mean Coriolis frequency in the area. Mean n_0 values for each season can be found in Table 2. We can see that the Prandtl ratios for the four study areas are of the same order of magnitude as the ones computed with the TOPAZ4 reanalysis (Table 1).

Table 2. Seasonal and yearly means of the Prandtl ratio n_0 within the study areas for the year 2018 using EN4 in-situ product.

Season	Winter	Spring	Summer	Autumn	Year Mean
Nordic Seas	37.47	47.69	71.51	48.97	51.36
Barents Sea	32.98	37.95	54.52	34.47	39.92
East Siberian Sea	119.14	114.01	145.26	131.04	127.28
Beaufort Sea	101.01	107.54	121.76	114.27	111.14

An example of the reconstructions from AVISO SLA for 28 August is shown in Figure 11. The main surface currents in the four study areas are reproduced. In summer, the Nordic Seas present (Figure 11a) a train of anticyclonic eddies towards the west of the location, where the Lofoten vortex resides (structure 2 in Figure 11). They seem to be over the Mohn Ridge, where the Norwegian Atlantic front current flows. In the winter image (Figure 11b), the Lofotonen vortex and other mesoscale eddies associated with the Norwegian Atlantic Current are present. The anticyclonic and cyclonic eddies along the FS that were visible in the reconstruction using reanalysis data (Figure 3), however, are not resolved here, in the reconstruction from remote sensing data (structures 3 and 4 in Figure 11). Higher mesoscale activity is found in winter along the East Greenland Shelf associated with the East Greenland Current, which was also present in the reconstruction from reanalysis data (Figure 3). The mesoscale structures in the Beaufort Sea (Figure 11c,d) are clearer in the image of 19 September than in the image corresponding to 20 March. This could be due to the fact that the region is covered by ice in March, whereas the free-of-ice area of the ocean surface is larger in September and, thus, more susceptible to atmospheric interactions. As a result, oceanic dynamics have more energy during the summer than they do during the winter. Moreover, although this SLA product includes coverage under the ice [66], the ice inhibits the satellite's ability to retrieve data, causing the SLA to be smoother than in ice-free areas. The anticyclonic eddy located at ∼72.2ºN and 159ºW (structure 4 in Figure 11) is clearly present for the image of 19 September as it was in the reconstruction from SSH reanalysis data (Figure 6a).

We compare the 3D reconstructions with the geostrophic currents derived from the in-situ EN4 data in order to validate the reconstructions that were derived from the AVISO SLA data. We compute the geostrophic velocities using EN4 salinity and temperature

in the water column applying Equations (11)–(13). Figure 12 displays the 3D reconstruction from SLA and the geostrophic velocities from in-situ ENK4 data in the Fram Strait (Figure 12a,b) and a section along the Beaufort Gyre (Figure 12c,d). Results exhibit compatible structures in the water column along the transect in the Fram Strait (latitude = 77.5°N) and the Beaufort Gyre (longitude = 159°W) between the AVISO SLA reconstructions and the geostrophic currents from in-situ EN4 data. In the transect along the Beaufort Gyre, the anticyclonic eddy presents a similar vertical structure as the one presented in the reconstructions from SSH reanalysis data (Figure 7a).

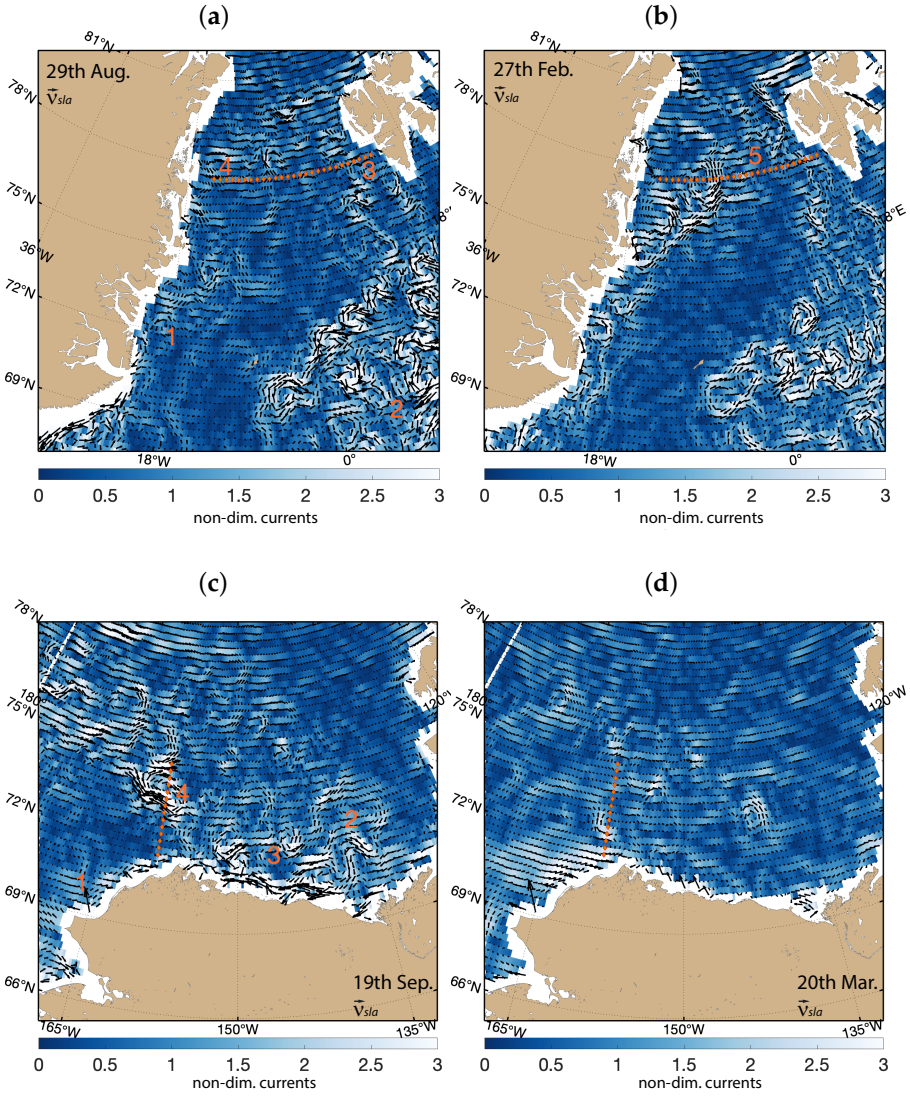

Figure 11. Example of normalized surface currents reconstructed from AVISO SLA in (**a**) Nordic Seas (for 29 August), (**b**) Nordic Seas (for 27 February), Fram Strait (FS) section at latitude 77.5°N in red diamonds, (**c**) Beaufort Sea (for 19 September), and (**d**) Beaufort Sea (for 20 March), Beaufort Gyre section at longitude 159°W in red diamonds.

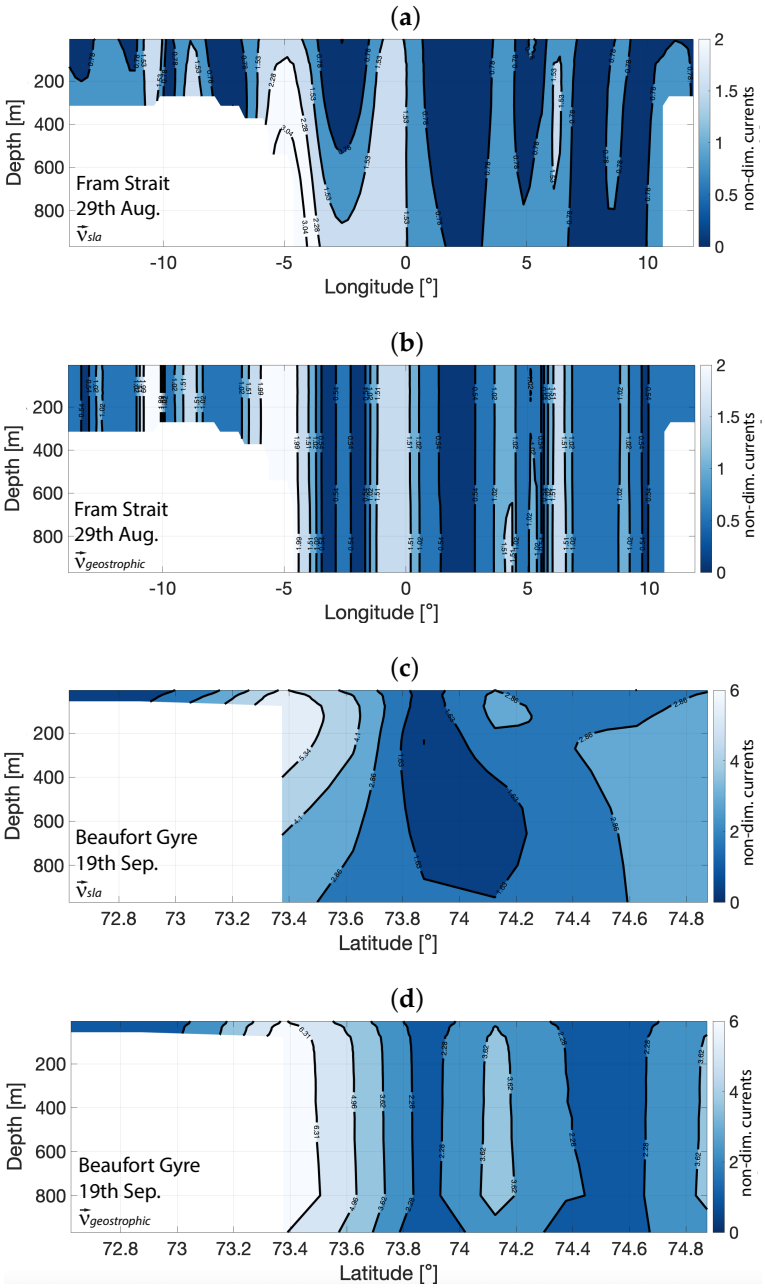

Figure 12. Normalized ocean currents reconstructed from AVISO SLA (**a**,**c**) and geostrophic velocities from in-situ EN4 data (**b**,**d**). Sections along Fram Strait (latitude = 77.5°N) for 29 August (**a**,**b**) and Beaufort Gyre (longitude = 159°W) for 19 September (**c**,**d**).

Figure 13 shows the correlations at each depth between the reconstructed vorticities from SLA as compared to those from EN4 geostrophic velocities. In the Nordic (Figure 13a) and Barents Seas (Figure 13b), the correlations are higher than 0.8 up to 800 m. August and September are the months with lower correlations and December and January present higher correlations. The East Siberian Sea (Figure 13c) shows the lowest performance, with correlations higher than 0.6 only up to 500 m. April and May are the months that show the highest correlation coefficients and July and August show the lowest correlation coefficients. The East Siberian is a shallow, highly stratified ocean, affected by river discharges and ice melting; therefore, we suggest that other components, apart from the geostrophic part, explain the upper ocean dynamics of the area.

The Beaufort Sea reconstruction from the surface sea level does agree with the geostrophic currents, exhibiting correlation coefficients higher than 0.6 up to 600 m (Figure 13d). The

Beaufort Sea exhibits correlation coefficients higher than 0.8 up to 300 m all year, and up to 400 m in February, March, and April. Note that the Beaufort Sea is a deeper sea than the East Siberian Sea, but also highly stratified. Higher correlation coefficients are observed in March and April, and lower correlation coefficients are found in July and August, as for the case of the East Siberian Sea.

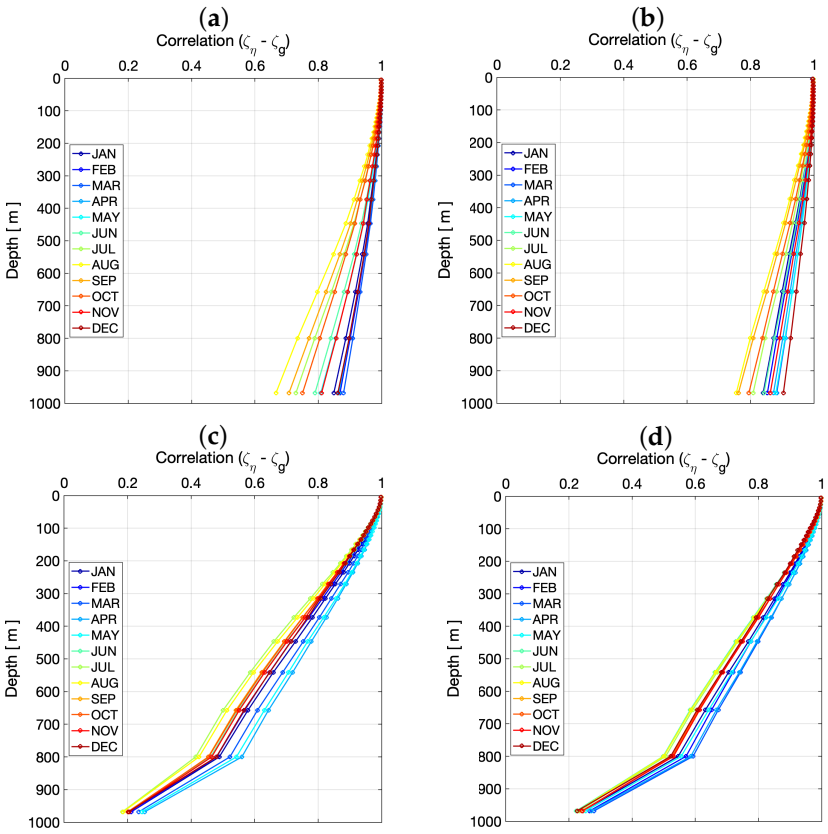

Figure 13. Positive correlations of relative vorticities between reconstruction from AVISO SLA with geostrophic velocities computed using EN4 in-situ measurements in (**a**) the Nordic Seas, (**b**) the Barents Sea, (**c**) the East Siberian Sea, and (**d**) the Beaufort Sea.

Previous research demonstrated that the SQG approach can recreate subsurface dynamics from remote sensing data in energetic regional locations [51,54]. This is the first attempt to implement this in the less energetic Arctic Seas. Our results using satellite data in the Arctic Seas indicate that the 3D dynamics can be reconstructed using only surface snapshots and a simple estimation of the stratification of the water column, yielding similar results to the geostrophic estimations based on the temperature and salinity information at each depth of the water column. Data assimilation into ocean circulation numerical models [64,88–90] or advanced statistical and machine learning algorithms [30,45,91–93] are alternatives that typically are more complex and numerically intensive methods for estimating the 3D state of the ocean from surface information. However, SQG is a computationally less consuming approach than a reanalysis system and can be used to develop new data assimilation techniques, diagnose the ocean dynamics in the upper layers, and reconstruct 3D dynamics from satellite data. Accurate reconstructions of upper ocean dynamics from surface data are essential to quantify the transfer of heat, freshwater, nutrients, plankton, oil spills, and debris in the changing Arctic Ocean. Refinement of the present results would require the inclusion of temperature and salinity data as a secondary component to that of altimetry, and the construction of the 3D dynamics from surface remote sensing products that combine SSH, SST, and SSS [94]. In addition, the essential

calibration of ocean current intensities derived from satellite data to match in-situ estimates remains a future research priority.

5. Conclusions

In this study, we evaluate the performance of a Surface Quasi-Geostrophic (SQG) approach in recreating three-dimensional ocean dynamics from sea surface information at high latitudes. Using the TOPAZ4 reanalysis system, we evaluate how well SQG works in four different Arctic regions. We also apply the approach to Sea Level Anomaly data obtained from remote sensing and validate it using in-situ EN4 data.

Using information from the TOPAZ4 system, we compare reconstructions derived from three surface variables. The first method is the reconstruction based on sea surface height (SSH), which is then applied to an altimetry product specifically developed from the Arctic Ocean. The second one is the reconstruction from surface buoyancy (SSB), which could be potentially applied to sea surface temperature (SST) and sea surface salinity (SSS) from passive radiometric missions. The final one is a reconstruction based on sea surface velocities (SSV), which could be applied in the near future, as SSV are going to be directly obtained in future satellite missions such as Seastar and WaCam.

Using the TOPAZ4 system, an evaluation of the effectiveness of the method is carried out. The results show that the SQG approach makes it possible to reconstruct three-dimensional dynamics in the Arctic Ocean by using only surface information, such as sea surface height or surface velocities, and information on the stratification of the water column; however, the approach is not able to reconstruct three-dimensional dynamics using only sea surface buoyancy. Accurate reconstructions (correlation coefficients greater than 0.8) are found up to 400 m in the Nordic Seas, up to 200 m in the Barents Seas, and up to 100 m in the Beaufort Sea, taking the geostrophic velocity from the TOPAZ4 system as a reference. Areas that are more stratified, such as the East Siberian Sea, hinder the reconstruction of the upper ocean dynamics from surface information, showing correlation coefficients greater than 0.6 only up to 100 m. Because there is less stratification in the water column during the winter and spring months, better 3D reconstructions are obtained during these seasons. Reconstructions from SSH cannot reproduce the non-geostrophic components in the total velocities from the reanalysis, while reconstructions from SSV are better correlated with the total velocity.

After the method is tested with TOPAZ4 outputs, it is applied to remotely sensed products of Sea Level Anomaly derived from AVISO that have been specifically tailored to the Arctic Ocean. This reconstruction shows correlation coefficients greater than 0.8 up to 400 m in depth compared with geostrophic velocities derived from in-situ EN4 data. The reconstructions from SLA are better in deeper and less stratified seas, as in the Nordic and Barents Seas, and more challenging in shallower platform seas, as in the East Siberian Sea.

This is the first time that the SQG approach is applied in the Arctic Ocean, obtaining successful reconstructions of the barotropic ocean dynamics from the surface to 400 m depth. The findings of this study demonstrate that the 3D dynamics of the upper ocean in polar regions can be retrieved with available remotely sensed altimetry information using SQG approaches, and it has the potential to be applied in the near future to remotely sensed SWOT and CRISTAL higher-resolution measurements of sea levels, even in the presence of sea ice, and Seastar and WaCM direct measurements of ocean surface currents. Combining the innovative and higher-resolution data provided by these recent and future missions with the available SQG methodologies will help to retrieve better-resolution 3D ocean dynamics from surface information in polar regions.

Author Contributions: Conceptualization, M.U. and J.I.-F.; methodology, M.U. and J.I.-F.; software, M.U. and J.I.-F.; validation, M.U.; formal analysis, M.U.; investigation, M.U. and M.G.; resources, M.U.; data curation, M.U. and L.B.; writing—original draft preparation, M.U. and E.D.-A.; writing—review and editing, R.G.-A., R.R., L.B. and C.G.; supervision, J.I.-F.; funding acquisition, M.U. All authors have read and agreed to the published version of the manuscript.

Funding: M. Umbert received funding from H2020 Marie Skłodowska-Curie Actions under Grant Agreement No. 840374. E. De Andrés received funding from the Margarita Salas Fellowship under Next-Generation EU Grant Agreement No. UP2021-035. This work has also been funded by the AEI with the ARCTIC-MON project (PID2021-125324OB-I00). This work represents a contribution to the CSIC Thematic Interdisciplinary Platform PTI-POLARCSIC and PTI-TELEDETECT. We also received funding from the Spanish government through the "Severo Ochoa Centre of Excellence" accreditation (CEX2019-000928-S) and from the ESA Arctic + Salinity Project (AO/1-9158/18/I-BG).

Conflicts of Interest: The authors declare no conflicts of interest.

References

1. Morison, J.; Kwok, R.; Peralta-Ferriz, C.; Alkire, M.; Rigor, I.; Andersen, R.; Steele, M. Changing arctic ocean freshwater pathways. *Nature* **2012**, *481*, 66–70. [CrossRef] [PubMed]
2. Haine, T.W.; Curry, B.; Gerdes, R.; Hansen, E.; Karcher, M.; Lee, C.; Rudels, B.; Spreen, G.; de Steur, L.; Stewart, K.D.; et al. Arctic freshwater export: Status, mechanisms, and prospects. *Glob. Planet. Chang.* **2015**, *125*, 13–35. [CrossRef]
3. Morison, J.; Kwok, R.; Dickinson, S.; Andersen, R.; Peralta-Ferriz, C.; Morison, D.; Rigor, I.; Dewey, S.; Guthrie, J. The Cyclonic Mode of Arctic Ocean Circulation. *J. Phys. Oceanogr.* **2021**, *51*, 1053–1075. [CrossRef]
4. Wang, Q.; Danilov, S.; Mu, L.; Sidorenko, D.; Wekerle, C. Lasting impact of winds on Arctic sea ice through the ocean's memory. *Cryosphere* **2021**, *15*, 4703–4725. [CrossRef]
5. Armitage, T.W.; Manucharyan, G.E.; Petty, A.A.; Kwok, R.; Thompson, A.F. Enhanced eddy activity in the Beaufort Gyre in response to sea ice loss. *Nat. Commun.* **2020**, *11*, 761. [CrossRef]
6. Petty, A.A.; Hutchings, J.K.; Richter-Menge, J.A.; Tschudi, M.A. Sea ice circulation around the Beaufort Gyre: The changing role of wind forcing and the sea ice state. *J. Geophys. Res. Ocean.* **2016**, *121*, 3278–3296. [CrossRef]
7. Campos, C.; Horn, M. The Physical System of the Arctic Ocean and Subarctic Seas in a Changing Climate. In *YOUMARES 8–Oceans Across Boundaries: Learning from Each Other*; Springer: Cham, Switzerland, 2018; pp. 25–40.
8. Comiso, J.C. A rapidly declining perennial sea ice cover in the Arctic. *Geophys. Res. Lett.* **2002**, *29*, 17-1–17-4. [CrossRef]
9. Cohen, J.; Screen, J.A.; Furtado, J.C.; Barlow, M.; Whittleston, D.; Coumou, D.; Francis, J.; Dethloff, K.; Entekhabi, D.; Overland, J.; et al. Recent Arctic amplification and extreme mid-latitude weather. *Nat. Geosci.* **2014**, *7*, 627–637. [CrossRef]
10. Timmermans, M.L.; Marshall, J. Understanding Arctic Ocean circulation: A review of ocean dynamics in a changing climate. *J. Geophys. Res. Ocean.* **2020**, *125*, e2018JC014378. [CrossRef]
11. Brakstad, A.; Våge, K.; Håvik, L.; Moore, G. Water mass transformation in the Greenland Sea during the period 1986–2016. *J. Phys. Oceanogr.* **2019**, *49*, 121–140. [CrossRef]
12. Rahmstorf, S. The thermohaline ocean circulation: A system with dangerous thresholds? *Clim. Chang.* **2000**, *46*, 247. [CrossRef]
13. Hansen, B.; Østerhus, S.; Quadfasel, D.; Turrell, W. Already the day after tomorrow? *Science* **2004**, *305*, 953–954. [CrossRef] [PubMed]
14. Blindheim, J.; Osterhus, S. The Nordic Seas, main oceanographic features. *Geophys.-Monogr.-Am. Geophys. Union* **2005**, *158*, 11.
15. Rudels, B.; Björk, G.; Nilsson, J.; Winsor, P.; Lake, I.; Nohr, C. The interaction between waters from the Arctic Ocean and the Nordic Seas north of Fram Strait and along the East Greenland Current: Results from the Arctic Ocean-02 Oden expedition. *J. Mar. Syst.* **2005**, *55*, 1–30. [CrossRef]
16. Shu, Q.; Wang, Q.; Song, Z.; Qiao, F. The poleward enhanced Arctic Ocean cooling machine in a warming climate. *Nat. Commun.* **2021**, *12*, 2966. [CrossRef]
17. Årthun, M.; Eldevik, T.; Smedsrud, L.H. The role of Atlantic heat transport in future Arctic winter sea ice loss. *J. Clim.* **2019**, *32*, 3327–3341. [CrossRef]
18. Anderson, L.G.; Andersson, P.S.; Björk, G.; Peter Jones, E.; Jutterström, S.; Wåhlström, I. Source and formation of the upper halocline of the Arctic Ocean. *J. Geophys. Res. Ocean.* **2013**, *118*, 410–421. [CrossRef]
19. Proshutinsky, A.; Bourke, R.; McLaughlin, F. The role of the Beaufort Gyre in Arctic climate variability: Seasonal to decadal climate scales. *Geophys. Res. Lett.* **2002**, *29*, 15-1–15-4. [CrossRef]
20. Balibrea-Iniesta, F.; Xie, J.; García-Garrido, V.J.; Bertino, L.; Mancho, A.M.; Wiggins, S. Lagrangian transport across the upper arctic waters in the Canada basin. *Q. J. R. Meteorol. Soc.* **2019**, *145*, 76–91. [CrossRef]
21. Pickart, R.S. Shelfbreak circulation in the Alaskan Beaufort Sea: Mean structure and variability. *J. Geophys. Res. Ocean.* **2004**, *109*. [CrossRef]
22. Zhang, J.; Weijer, W.; Steele, M.; Cheng, W.; Verma, T.; Veneziani, M. Labrador Sea freshening linked to Beaufort Gyre freshwater release. *Nat. Commun.* **2021**, *12*, 1229. [CrossRef] [PubMed]
23. Morison, J.; Kwok, R.; Rigor, I. Changes in Arctic Ocean Circulation from In Situ and Remotely Sensed Observations. *Oceanography* **2022**, *35*, 57. [CrossRef]
24. Kelly, S.; Proshutinsky, A.; Popova, E.; Aksenov, Y.; Yool, A. On the origin of water masses in the Beaufort Gyre. *J. Geophys. Res. Ocean.* **2019**, *124*, 4696–4709. [CrossRef]

25. Proshutinsky, A.; Krishfield, R.; Toole, J.; Timmermans, M.L.; Williams, W.; Zimmermann, S.; Yamamoto-Kawai, M.; Armitage, T.; Dukhovskoy, D.; Golubeva, E.; et al. Analysis of the Beaufort Gyre freshwater content in 2003–2018. *J. Geophys. Res. Ocean.* **2019**, *124*, 9658–9689. [CrossRef]
26. Röhrs, J.; Sutherland, G.; Jeans, G.; Bedington, M.; Sperrevik, A.K.; Dagestad, K.F.; Gusdal, Y.; Mauritzen, C.; Dale, A.; LaCasce, J.H. Surface currents in operational oceanography: Key applications, mechanisms, and methods. *J. Oper. Oceanogr.* **2023**, *16*, 60–88. [CrossRef]
27. Reul, N.; Grodsky, S.; Arias, M.; Boutin, J.; Catany, R.; Chapron, B.; d'Amico, F.; Dinnat, E.; Donlon, C.; Fore, A.; et al. Sea surface salinity estimates from spaceborne L-band radiometers: An overview of the first decade of observation (2010–2019). *Remote. Sens. Environ.* **2020**, *242*, 111769. [CrossRef]
28. Martínez, J.; Gabarró, C.; Turiel, A.; González-Gambau, V.; Umbert, M.; Hoareau, N.; González-Haro, C.; Olmedo, E.; Arias, M.; Catany, R.; et al. Improved BEC SMOS Arctic Sea surface salinity product v3. 1. *Earth Syst. Sci. Data* **2022**, *14*, 307–323. [CrossRef]
29. Dohan, K.; Maximenko, N. Monitoring ocean currents with satellite sensors. *Oceanography* **2010**, *23*, 94–103. [CrossRef]
30. Rio, M.H.; Santoleri, R.; Bourdalle-Badie, R.; Griffa, A.; Piterbarg, L.; Taburet, G. Improving the altimeter-derived surface currents using high-resolution sea surface temperature data: A feasability study based on model outputs. *J. Atmos. Ocean. Technol.* **2016**, *33*, 2769–2784. [CrossRef]
31. Chelton, D.B.; DeSzoeke, R.A.; Schlax, M.G.; El Naggar, K.; Siwertz, N. Geographical variability of the first baroclinic Rossby radius of deformation. *J. Phys. Oceanogr.* **1998**, *28*, 433–460. [CrossRef]
32. Nurser, A.; Bacon, S. The rossby radius in the arctic ocean. *Ocean. Sci.* **2014**, *10*, 967–975. [CrossRef]
33. Pascual, A.; Faugere, Y.; Larnicol, G.; LeTraon, P. Improved description of the ocean mesoscale variability by combining four satellite altimeters. *Geophys. Res. Lett* **2006**, *33*, 611. [CrossRef]
34. Ballarotta, M.; Ubelmann, C.; Pujol, M.I.; Taburet, G.; Fournier, F.; Legeais, J.F.; Faugère, Y.; Delepoulle, A.; Chelton, D.; Dibarboure, G.; et al. On the resolutions of ocean altimetry maps. *Ocean. Sci.* **2019**, *15*, 1091–1109. [CrossRef]
35. Pujol, M.I.; Schaeffer, P.; Faugère, Y.; Raynal, M.; Dibarboure, G.; Picot, N. Gauging the improvement of recent mean sea surface models: A new approach for identifying and quantifying their errors. *J. Geophys. Res. Ocean.* **2018**, *123*, 5889–5911. [CrossRef]
36. Armitage, T.W.; Bacon, S.; Ridout, A.L.; Thomas, S.F.; Aksenov, Y.; Wingham, D.J. Arctic sea surface height variability and change from satellite radar altimetry and GRACE, 2003–2014. *J. Geophys. Res. Ocean.* **2016**, *121*, 4303–4322. [CrossRef]
37. Villas Bôas, A.B.; Ardhuin, F.; Ayet, A.; Bourassa, M.A.; Brandt, P.; Chapron, B.; Cornuelle, B.D.; Farrar, J.T.; Fewings, M.R.; Fox-Kemper, B.; et al. Integrated observations of global surface winds, currents, and waves: Requirements and challenges for the next decade. *Front. Mar. Sci.* **2019**, *6*, 425. [CrossRef]
38. Gommenginger, C.; Chapron, B.; Hogg, A.; Buckingham, C.; Fox-Kemper, B.; Eriksson, L.; Soulat, F.; Ubelmann, C.; Ocampo-Torres, F.; Nardelli, B.B.; et al. SEASTAR: A mission to study ocean submesoscale dynamics and small-scale atmosphere-ocean processes in coastal, shelf and polar seas. *Front. Mar. Sci.* **2019**, *6*, 457. [CrossRef]
39. Ciani, D.; Santoleri, R.; Liberti, G.L.; Prigent, C.; Donlon, C.; Buongiorno Nardelli, B. Copernicus Imaging Microwave Radiometer (CIMR) Benefits for the Copernicus Level 4 Sea-Surface Salinity Processing Chain. *Remote Sens.* **2019**, *11*, 1818. [CrossRef]
40. Rodríguez, E.; Bourassa, M.; Chelton, D.; Farrar, J.T.; Long, D.; Perkovic-Martin, D.; Samelson, R. The winds and currents mission concept. *Front. Mar. Sci.* **2019**, *6*, 438. [CrossRef]
41. Chelton, D.B.; Schlax, M.G.; Samelson, R.M.; Farrar, J.T.; Molemaker, M.J.; McWilliams, J.C.; Gula, J. Prospects for future satellite estimation of small-scale variability of ocean surface velocity and vorticity. *Prog. Oceanogr.* **2019**, *173*, 256–350. [CrossRef]
42. Chelton, D.B.; Samelson, R.M.; Farrar, J.T. The Effects of Uncorrelated Measurement Noise on SWOT Estimates of Sea-Surface Height, Velocity and Vorticity. *J. Atmos. Ocean. Technol.* **2022**, *39*, 1053–1083. [CrossRef]
43. Kern, M.; Cullen, R.; Berruti, B.; Bouffard, J.; Casal, T.; Drinkwater, M.R.; Gabriele, A.; Lecuyot, A.; Ludwig, M.; Midthassel, R.; et al. The Copernicus Polar Ice and Snow Topography Altimeter (CRISTAL) high-priority candidate mission. *Cryosphere* **2020**, *14*, 2235–2251. [CrossRef]
44. Buongiorno, B. A Novel Approach for the High-Resolution Interpolation of In Situ Sea Surface Salinity. *J. Atmos. Ocean. Technol.* **2012**, *29*, 867–879.
45. Buongiorno Nardelli, B.; Mulet, S.; Iudicone, D. Three-dimensional ageostrophic motion and water mass subduction in the Southern Ocean. *J. Geophys. Res. Ocean.* **2018**, *123*, 1533–1562. [CrossRef]
46. Lapeyre, G.; Klein, P. Dynamics of the Upper Oceanic Layers in Terms of Surface Quasigeostrophy Theory. *J. Phys. Oceanogr.* **2006**, *36*, 165–176. [CrossRef]
47. LaCasce, J.; Mahadevan, A. Estimating subsurface horizontal and vertical velocities from sea-surface temperature. *J. Mar. Res.* **2006**, *64*, 695–721. [CrossRef]
48. Isern-Fontanet, J.; Shinde, M.; González-Haro, C. On the transfer function between surface fields and the geostrophic stream function in the Mediterranean Sea. *J. Phys. Oceanogr.* **2014**, *44*, 1406–1423. [CrossRef]
49. Isern-Fontanet, J.; García-Ladona, E.; Jiménez-Madrid, J.A.; Olmedo, E.; García-Sotillo, M.; Orfila, A.; Turiel, A. Real-time reconstruction of surface velocities from satellite observations in the Alboran sea. *Remote Sens.* **2020**, *12*, 724. [CrossRef]
50. Isern-Fontanet, J.; García-Ladona, E.; González-Haro, C.; Turiel, A.; Rosell-Fieschi, M.; Company, J.B.; Padial, A. High-Resolution Ocean Currents from Sea Surface Temperature Observations: The Catalan Sea (Western Mediterranean). *Remote Sens.* **2021**, *13*, 3635. [CrossRef]

51. Isern-Fontanet, J.; Chapron, B.; Lapeyre, G.; Klein, P. Potential use of microwave sea surface temperatures for the estimation of ocean currents. *Geophys. Res. Lett.* **2006**, *22*, L24608. [CrossRef]
52. González-Haro, C.; Isern-Fontanet, J. Global ocean current reconstruction from altimetric and microwave SST measurements. *J. Geophys. Res. Ocean.* **2014**, *119*, 3378–3391. [CrossRef]
53. Isern-Fontanet, J.; Olmedo, E.; Turiel, A.; Ballabrera-Poy, J.; García-Ladona, E. Retrieval of eddy dynamics from SMOS sea surface salinity measurements in the Algerian Basin (Mediterranean Sea). *Geophys. Res. Lett.* **2016**, *43*, 6427–6434. [CrossRef]
54. Isern-Fontanet, J.; Lapeyre, G.; Klein, P.; Chapron, B.; Hecht, M.W. Three-dimensional reconstruction of oceanic mesoscale currents from surface information. *J. Geophys. Res. Ocean.* **2008**, *113* . [CrossRef]
55. Miracca-Lage, M.; González-Haro, C.; Napolitano, D.C.; Isern-Fontanet, J.; Polito, P.S. Can the Surface Quasi-Geostrophic (SQG) Theory Explain Upper Ocean Dynamics in the South Atlantic? *J. Geophys. Res. Ocean.* **2022**, *127*, e2021JC018001. [CrossRef]
56. Wang, J.; Flierl, G.R.; LaCasce, J.H.; McClean, J.L.; Mahadevan, A. Reconstructing the ocean's interior from surface data. *J. Phys. Oceanogr.* **2013**, *43*, 1611–1626. [CrossRef]
57. LaCasce, J.H.; Wang, J. Estimating subsurface velocities from surface fields with idealized stratification. *J. Phys. Oceanogr.* **2015**, *45*, 2424–2435. [CrossRef]
58. de La Lama, M.S.; LaCasce, J.; Fuhr, H.K. The vertical structure of ocean eddies. *Dyn. Stat. Clim. Syst.* **2016**, 1, dzw001. [CrossRef]
59. Lapeyre, G. Surface quasi-geostrophy. *Fluids* **2017**, *2*, 7. [CrossRef]
60. Lacasce, J.H. The prevalence of oceanic surface modes. *Geophys. Res. Lett.* **2017**, *44*, 11–097. [CrossRef]
61. Klein, P.; Isern-Fontanet, J.; Lapeyre, G.; Roullet, G.; Danioux, E.; Chapron, B.; Le Gentil, S.; Sasaki, H. Diagnosis of vertical velocities in the upper ocean from high resolution sea surface height. *Geophys. Res. Lett.* **2009**, *36*, L12603. [CrossRef]
62. Isern-Fontanet, J.; Hascoët, E. Diagnosis of high-resolution upper ocean dynamics from noisy sea surface temperatures. *J. Geophys. Res. Ocean.* **2014**, *119*, 121–132. [CrossRef]
63. Buongiorno Nardelli, B. A multi-year time series of observation-based 3D horizontal and vertical quasi-geostrophic global ocean currents. *Earth Syst. Sci. Data* **2020**, *12*, 1711–1723. [CrossRef]
64. Stammer, D.; Balmaseda, M.; Heimbach, P.; Köhl, A.; Weaver, A. Ocean data assimilation in support of climate applications: Status and perspectives. *Annu. Rev. Mar. Sci.* **2016**, *8*, 491–518. [CrossRef]
65. Xie, J.; Bertino, L.; Counillon, F.; Lisæter, K.A.; Sakov, P. Quality assessment of the TOPAZ4 reanalysis in the Arctic over the period 1991–2013. *Ocean Sci.* **2017**, *13*, 123–144. [CrossRef]
66. Prandi, P.; Poisson, J.C.; Faugère, Y.; Guillot, A.; Dibarboure, G. Arctic sea surface height maps from multi-altimeter combination. *Earth Syst. Sci. Data* **2021**, *13*, 5469–5482. [CrossRef]
67. Good, S.A.; Martin, M.J.; Rayner, N.A. EN4: Quality controlled ocean temperature and salinity profiles and monthly objective analyses with uncertainty estimates. *J. Geophys. Res. Ocean.* **2013**, *118*, 6704–6716. [CrossRef]
68. Hoskins, B.J.; McIntyre, M.E.; Robertson, A.W. On the use and significance of isentropic potential vorticity maps. *Q. J. R. Meteorol. Soc.* **1985**, *111*, 877–946. [CrossRef]
69. Wright, D.; Pawlowicz, R.; McDougall, T.; Feistel, R.; Marion, G. Absolute Salinity, "Density Salinity" and the Reference-Composition Salinity Scale: Present and future use in the seawater standard TEOS-10. *Ocean Sci.* **2011**, *7*, 1–26. [CrossRef]
70. González-Haro, C.; Isern-Fontanet, J.; Tandeo, P.; Garello, R. Ocean surface currents reconstruction: Spectral characterization of the transfer function between SST and SSH. *J. Geophys. Res. Ocean* **2020**, *125*, e2019JC015958. [CrossRef]
71. Held, I.M.; Pierrehumbert, R.T.; Garner, S.T.; Swanson, K.L. Surface quasi-geostrophic dynamics. *J. Fluid Mech.* **1995**, *282*, 1–20. [CrossRef]
72. Tulloch, R.; Smith, K. A theory for the atmospheric energy spectrum: Depth-limited temperature anomalies at the tropopause. *Proc. Natl. Acad. Sci. USA* **2006**, *103*, 14690–14694. [CrossRef] [PubMed]
73. Vallis, G.K. *Atmospheric and Oceanic Fluid Dynamics*; Cambridge University Press: Cambridge, UK, 2017.
74. Wang, Q.; Wekerle, C.; Danilov, S.; Wang, X.; Jung, T. A 4.5 km resolution Arctic Ocean simulation with the global multi-resolution model FESOM 1.4. *Geosci. Model Dev.* **2018**, *11*, 1229–1255. [CrossRef]
75. Stedmon, C.A.; Amon, R.M.; Bauch, D.; Bracher, A.; Gonçalves-Araujo, R.; Hoppmann, M.; Krishfield, R.; Laney, S.; Rabe, B.; Reader, H.; et al. Insights Into Water Mass Origins in the Central Arctic Ocean From In-Situ Dissolved Organic Matter Fluorescence. *J. Geophys. Res. Ocean.* **2021**, *126*, e2021JC017407. [CrossRef]
76. Raj, R.P.; Chafik, L.; Nilsen, J.E.Ø.; Eldevik, T.; Halo, I. The Lofoten vortex of the Nordic seas. *Deep. Sea Res. Part I Oceanogr. Res. Pap.* **2015**, *96*, 1–14. [CrossRef]
77. Richards, C.G.; Straneo, F. Observations of water mass transformation and eddies in the Lofoten Basin of the Nordic Seas. *J. Phys. Oceanogr.* **2015**, *45*, 1735–1756. [CrossRef]
78. Ivanov, V.V.; Korablev, A.A. Formation and regeneration of the pycnocline lens in the Norwegian Sea. *Russ. Meteor. Hydrol.* **1995**, *9*, 62–69.
79. Köhl, A. Generation and stability of a quasi-permanent vortex in the Lofoten Basin. *J. Phys. Oceanogr.* **2007**, *37*, 2637–2651. [CrossRef]
80. Trodahl, M.; Isachsen, P.E.; Lilly, J.M.; Nilsson, J.; Kristensen, N.M. The regeneration of the Lofoten Vortex through vertical alignment. *J. Phys. Oceanogr.* **2020**, *50*, 2689–2711. [CrossRef]
81. Wekerle, C.; Wang, Q.; von Appen, W.J.; Danilov, S.; Schourup-Kristensen, V.; Jung, T. Eddy-resolving simulation of the Atlantic water circulation in the Fram Strait with focus on the seasonal cycle. *J. Geophys. Res. Ocean.* **2017**, *122*, 8385–8405. [CrossRef]

82. Bashmachnikov, I.L.; Kozlov, I.E.; Petrenko, L.A.; Glok, N.I.; Wekerle, C. Eddies in the North Greenland Sea and Fram Strait from satellite altimetry, SAR and high-resolution model data. *J. Geophys. Res. Ocean.* **2020**, *125*, e2019JC015832. [CrossRef]
83. Yuan, M.; Song, Z.; Jing, Z.; Li, Z.; Wu, L. Distinct roles of global cyclonic and anticyclonic eddies in regulating near-inertial internal waves in the ocean interior. *Front. Mar. Sci.* **2022**, *9*, 1624. [CrossRef]
84. Timmermans, M.L.; Toole, J.M. The Arctic Ocean's Beaufort Gyre. *Annu. Rev. Mar. Sci.* **2023**, *15*, 223–248. [CrossRef] [PubMed]
85. Kubryakov, A.; Kozlov, I.; Manucharyan, G. Large mesoscale eddies in the Western Arctic Ocean from satellite altimetry measurements. *J. Geophys. Res. Ocean.* **2021**, *126*, e2020JC016670. [CrossRef]
86. Rio, M.H.; Mulet, S.; Picot, N. Beyond GOCE for the ocean circulation estimate: Synergetic use of altimetry, gravimetry, and in situ data provides new insight into geostrophic and Ekman currents. *Geophys. Res. Lett.* **2014**, *41*, 8918–8925. [CrossRef]
87. Ciani, D.; Rio, M.H.; Nardelli, B.B.; Etienne, H.; Santoleri, R. Improving the altimeter-derived surface currents using sea surface temperature (SST) data: A sensitivity study to SST products. *Remote Sens.* **2020**, *12*, 1601. [CrossRef]
88. Wunsch, C.; Heimbach, P. Dynamically and kinematically consistent global ocean circulation and ice state estimates. In *International Geophysics*; Elsevier: Amsterdam, The Netherlands, 2013; Volume 103, pp. 553–579.
89. Moore, A.M.; Martin, M.J.; Akella, S.; Arango, H.G.; Balmaseda, M.; Bertino, L.; Ciavatta, S.; Cornuelle, B.; Cummings, J.; Frolov, S.; et al. Synthesis of ocean observations using data assimilation for operational, real-time and reanalysis systems: A more complete picture of the state of the ocean. *Front. Mar. Sci.* **2019**, *6*, 90. [CrossRef]
90. Janeković, I.; Rayson, M.; Jones, N.; Watson, P.; Pattiaratchi, C. 4D-Var data assimilation using satellite sea surface temperature to improve the tidally-driven interior ocean dynamics estimates in the Indo-Australian Basin. *Ocean Model.* **2022**, *171*, 101969. [CrossRef]
91. Nardelli, B.B.; Santoleri, R. Methods for the reconstruction of vertical profiles from surface data: Multivariate analyses, residual GEM, and variable temporal signals in the North Pacific Ocean. *J. Atmos. Ocean. Technol.* **2005**, *22*, 1762–1781. [CrossRef]
92. Buongiorno Nardelli, B.; Guinehut, S.; Pascual, A.; Drillet, Y.; Ruiz, S.; Mulet, S. Towards high resolution mapping of 3-D mesoscale dynamics from observations. *Ocean Sci.* **2012**, *8*, 885–901. [CrossRef]
93. Mulet, S.; Rio, M.H.; Mignot, A.; Guinehut, S.; Morrow, R. A new estimate of the global 3D geostrophic ocean circulation based on satellite data and in-situ measurements. *Deep. Sea Res. Part II Top. Stud. Oceanogr.* **2012**, *77*, 70–81. [CrossRef]
94. Umbert, M.; Guimbard, S.; Lagerloef, G.; Thompson, L.; Portabella, M.; Ballabrera-Poy, J.; Turiel, A. Detecting the surface salinity signature of Gulf Stream cold-core rings in Aquarius synergistic products. *J. Geophys. Res. Ocean.* **2015**, *120*, 859–874. [CrossRef]

Disclaimer/Publisher's Note: The statements, opinions and data contained in all publications are solely those of the individual author(s) and contributor(s) and not of MDPI and/or the editor(s). MDPI and/or the editor(s) disclaim responsibility for any injury to people or property resulting from any ideas, methods, instructions or products referred to in the content.